

NO EVIDENCE FOR THE AQUARIUS CO-MOVING GROUP RESULTING FROM A DISRUPTED CLASSICAL GLOBULAR CLUSTER¹

ANDREW R. CASEY^{2,3}, STEFAN KELLER², ALAN ALVES-BRITO², ANNA FREBEL³, GARY DA COSTA², KEVIN SCHALUFMAN³,
 AMANDA KARAKAS², DAVID YONG², HEATHER JACOBSON³, QINQIN YU³, KEN FREEMAN²

Draft version February 19, 2013

ABSTRACT

We present a detailed analysis of five Aquarius stream candidate stars observed using the MIKE spectrograph with the Magellan Clay telescope. Enhanced [Na/Fe] and [Ni/Fe] abundance ratios suggest the co-moving group is not the result of a dwarf satellite galaxy, and that its chemical enrichment environment is more representative of either a globular cluster, or the Milky Way thick disc. However, we find no evidence that the stream is a result of a classical disrupted globular cluster. Our data indicate the Aquarius stream has a metallicity dispersion of $\sigma([\text{Fe}/\text{H}]) = 0.32$ dex, ranging between $[\text{Fe}/\text{H}] = -0.65$ to -1.60 dex. No inverse Na-O correlation is present, and we find a positive Mg-Al relationship. Chemically, the group is indistinguishable from the Milky Way thick disk/halo with the exception of one very interesting candidate, which we hypothesise is tidal debris from ω -Centauri. Assuming all other candidates are Aquarius members, we propose the co-moving group has arisen from a minor merger in the Milky Way's thick disk.

Subject headings: Galaxy: halo, structure

1. INTRODUCTION

Galaxies are hierarchically formed through chaotic mergers of smaller systems. The Milky Way is no exception. The accumulating stellar debris in our own galactic halo provides ongoing evidence for such merging events. As accreting satellites infall onto the galaxy, tidal forces disrupt the dwarf, hurtling stars in leading and trailing directions. Unsurprisingly, the velocities of stars within these ‘stellar streams’ are sensitive to the galactic potential. As such, their phase-space information can collectively constrain the fraction and distribution of accreted matter in the galaxy, the sub-halo mass function, as well as the shape and extent of dark matter in the Milky Way. Moreover, individual chemical abundances can trace the chemical evolution of the galaxy.

Wide-field imaging surveys have proved excellent sources for finding stellar streams. Dozens have been identified through photometric selections and matched-filtering techniques, with some to a galactocentric distance of 100 kpc (Belokurov et al. 2007; Drake et al. 2013). Indeed, it is clear that a large fraction of the stellar halo has been built up by accretion. However, as Helmi & White (1999) point out, these observing strategies are only successful for identifying streams that are sufficiently distant from the solar neighbourhood. A nearby stream, within ~ 10 kpc, will not appear as an over-density as the stars would be sparsely positioned across the sky. Such substructures would only be detectable by their kinematics, or perhaps with precise chemical abundances through a ‘chemical tagging’ approach (e.g. see Freeman & Bland-Hawthorn (2002)).

It is therefore necessary to survey solar neighbourhood stars with spectroscopy to reveal any nearby substructures. The RAVE (Radial Velocity Experiment) team began such a survey in 2003 and have observed spectra from over 500,000 stars across 17,000 deg². As the name hints, the primary goal of RAVE was to obtain radial velocities for the solar neighbourhood and beyond. In an attempt to remain kinematically unbiased, RAVE candidates were selected based only on their apparent magnitude. With the exception of bulge stars, where some photometric cuts were employed, all stars between $9 < I < 13$ were observed. Almost all of these candidates have published radial velocity measurements (Steinmetz et al. 2006), and for a subset of stars with a sufficient Signal-to-Noise (S/N) ratio, estimates of stellar parameters have been derived using a χ^2 minimization technique (Zwitter et al. 2008; Siebert et al. 2011).

Using these data, Williams et al. (2011) identified a co-moving group of nearby ($0.5 \text{ kpc} \lesssim d \lesssim 10 \text{ kpc}$) stars in the vicinity of the Aquarius constellation ($l, b = (60^\circ, -55^\circ)$). Thus, the co-moving group was named the Aquarius stream. The group is most apparent when examining velocities against galactic latitude for stars within $-70^\circ < b < -50^\circ$. Williams et al. (2011) employed a selection criteria of $-250 \text{ km s}^{-1} < V_{\text{hel}} < -150 \text{ km s}^{-1}$, $30^\circ < l < 75^\circ$ and $J > 10.3$ to maximize the contrast between the stream and background, identifying 15 candidates in the process. The average heliocentric velocity of these members was found to be $V_{\text{hel}} = -199 \text{ km s}^{-1}$, with a dispersion of 27 km s^{-1} . The radial velocity uncertainties provided by the RAVE catalog are described to be $\sim 2 \text{ km s}^{-1}$, so the wide kinematic distribution appears to be real.

Upon examining the galactic longitude and velocities of Aquarius stars, the stream appears quite distinct from the halo. In order to quantify the statistical likelihood that the Aquarius stream is truly separate from a smooth halo distribution, Williams et al. (2011)

¹ This paper includes data gathered with the 6.5 meter Magellan Telescopes located at Las Campanas Observatory, Chile.

² Research School of Astronomy & Astrophysics, Australian National University, Mount Stromlo Observatory, via Cotter Rd, Weston, ACT 2611, Australia; acasey@mso.anu.edu.au

³ Massachusetts Institute of Technology, Kavli Institute for Astrophysics and Space Research, 77 Massachusetts Avenue, Cambridge, MA 02139, USA

compared the number of observed RAVE stars within $-70^\circ < b < -50^\circ$ against the Galaxia (Sharma et al. 2011) and Besançon (Robin et al. 2003) galaxy simulations. The predicted particles in each model between $-70^\circ < b < -50^\circ$ were binned in $\Delta l \times \Delta V_{\text{hel}}$ blocks using varying grid cell sizes between 25° to 70° and 20 km s^{-1} to 100 km s^{-1} . The RAVE sample was binned in the same way, discretizing the statistical significance of the observed over-density. Williams et al. (2011) found the stream to be statistically significant ($>4\sigma$) in 96% of the cell proportions employed for the Besançon model. By sampling the Galaxia model repeatedly with varying extinction rates, a similar result was found: between $75 \pm 15\%$ to $80 \pm 18\%$ of grid cells showed the Aquarius stream to be significant at the 4σ level or higher. Given the high-latitude and proximity of the stream, it is not surprising that dust had a negligible effect on the statistical significance. Williams et al. (2011) concluded that the over-density in l, V_{hel} is a true substructure, and neither the choice of galaxy model, cell dimension, nor the extinction rate made any real difference to the detection significance.

The Sagittarius stream is arguably the most prominent ongoing accretion event in the galaxy. Given the extent of stellar debris the dwarf has littered throughout the Milky Way, it is reasonable to suspect the Aquarius stream might originate from the Sagittarius dwarf. Indeed, the Aquarius stars do not lie far from the orbital plane of Sagittarius, and the metallicities reported by Williams et al. (2011) are not dissimilar from the Sagittarius stream. However, Williams et al. (2011) found the Aquarius transverse motions (specifically V_Z and V_ϕ) to be quite distinct from Sagittarius. Based on the phase space information available, Williams et al. (2011) concluded that the newly discovered stream could not be positively associated with the Monoceros stream, Hercules-Aquila cloud, or either the Canis Major or Virgo over-densities.

RAVE observations suggest the Aquarius stream has a metallicity of $[\text{Fe}/\text{H}] \sim -1.0$, slightly more metal-rich than halo stars at the same distance. Williams et al. (2011) found the stream to have an average of $[\text{M}/\text{H}] = -1.0 \pm 0.4$, compared to $[\text{M}/\text{H}] = -1.1 \pm 0.6$ for background stars after the same selection cuts had been employed. Of the 12 Aquarius stars in the Williams et al. (2011) discovery sample with stellar parameters, the metallicity range is wide: between -2.02 and -0.33 dex. Spectroscopic observations of high resolution with high S/N are necessary to accurately characterize the stream's metallicity distribution.

To this end, Wylie-de Boer et al. (2012) obtained high-resolution ($R = 25,000$) spectra with modest S/N ($\sim 30 \text{ pixel}^{-1}$) for six Aquarius stream stars. Their data indicate a very narrow metallicity distribution: $[\text{Fe}/\text{H}] = -1.09 \pm 0.10$ dex extending between $[\text{Fe}/\text{H}] = -1.25$ to -0.98 dex. Observations of such minimal chemical scatter from stars with a common origin is typically noted in either globular, or open clusters. The largest $[\text{Fe}/\text{H}]$ discrepancy between the Williams et al. (2011) and Wylie-de Boer et al. (2012) study was $\Delta[\text{Fe}/\text{H}] = -0.66$ dex for the most metal-rich star in the Williams et al. (2011) sample. The most metal-poor star in the Williams et al. (2011) study was not observed by Wylie-de Boer et al.

(2012).

In addition to ascertaining stellar parameters, Wylie-de Boer et al. (2012) measured elemental abundances for the Aquarius stream stars – the only study to do so until now. The authors primarily focussed on light elements: Na, O, Ni, Mg, and Al. Chemical patterns in these light elements arise as natural consequences of nucleosynthetic processes in massive stars. These patterns have been repeatedly observed in globular clusters. Specifically, an anti-correlation between sodium and oxygen content appears ubiquitous to globular clusters. While the exact formation site is still under debate, the chemical relationship is well-established empirically. The Na-O pattern provides the best chemical evidence that their enrichment history has been dominated by Type II Supernova (SN) events, and that those stars formed in a globular cluster-like environment.

From high-resolution spectroscopy of six candidate Aquarius stars, four of which have sodium and oxygen abundance measurements, Wylie-de Boer et al. (2012) found two stars with super-solar sodium; slightly higher $[\text{Na}/\text{Fe}]$ ratios than halo stars of the same metallicity. However, no strong oxygen depletion was evident in the data. Thus, they observed no evidence of a classical Na-O inverse correlation in the Aquarius stream.

There are other chemical abundance patterns that allow us to infer the chemical enrichment environment. Nissen & Schuster (1997) first noted that nearby solar neighbourhood stars were enriched in $[\text{Ni}/\text{Fe}]$ and $[\text{Na}/\text{Fe}]$. Fulbright (2000) came to a similar conclusion: only somewhat distant ($R_\odot > 20 \text{ kpc}$) stars are likely to be sodium deficient. If the stellar halo has been built up from the accretion of smaller dwarf satellites, Nissen & Schuster (1997) proposed that this chemical trend may be indicative of the halo merger history since stars at larger R_\odot are more likely to have been accreted rather than formed in-situ. Wylie-de Boer et al. (2012) found all the Aquarius stars in their sample to be enriched in both sodium and nickel; contrary to what would be expected if the stars originated from a disrupted dwarf spheroidal (dSph) galaxy. This provided an additional indication that the Aquarius stream stars originated in a globular cluster-like environment.

Combined with the low level of chemical scatter present in their sample, these chemical indicators led Wylie-de Boer et al. (2012) to conclude that the Aquarius stream is the result of a tidally disrupted globular cluster. Williams et al. (2011) had previously precluded this possibility with any known clusters after modelling an Aquarius-like progenitor infalling onto the Milky Way and comparing the predicted l, b, V_{hel} with known, nearby globular clusters of similar metallicities. No known globular cluster could match their simulation. If both scenarios are accurate then the undiscovered disrupting cluster might still remain, and would be relatively close by.

We seek to investigate the nature of the Aquarius stream, specifically the recent globular cluster origin claim made by Wylie-de Boer et al. (2012). We present a detailed analysis for five Aquarius stream candidates from high-resolution, high S/N observations taken using the Magellan Inamori Kyocera Echelle spectrograph (Bernstein et al. 2003) with the Magellan Clay telescope. Details of the observations and data reduction are outlined in the following section. The data analysis is chron-

icled in Section 3 and a detailed discussion of these results resides in Section 4. In Section 5 we present our conclusions and critical interpretations.

2. OBSERVATIONS & DATA REDUCTION

The most complete sample of Aquarius stream stars is presented in the discovery paper of Williams et al. (2011). Our sample includes five stars: four common to the Wylie-de Boer et al. (2012) study, and an additional candidate from the original Williams et al. (2011) sample. The supplementary star, J2306265-085103, was observed by the RAVE survey but had a S/N ratio too low for stellar parameters to be accurately determined. All program stars were observed in July 2011 in good seeing at low airmass (Table 1), and six standard stars were observed in March 2011. All observations were taken using a $1.0''$ slit, providing a spectral resolution of $\mathcal{R} = 28,000$ in the blue arm and $\mathcal{R} = 22,000$ in the red arm. The exposure time for our program stars was 650 s, in order to ensure a S/N ratio in excess of 100 pixel^{-1} at 600 nm.

Calibration frames were taken at the start of each night, including twenty flat-field frames (10 quartz, 10 milky) and 10 Th-Ar arc lamp exposures for wavelength calibration. The data were reduced using the CarPy pipeline⁴. One standard star, HD 41667, was also reduced using standard extraction and calibration methods in IRAF. The resultant spectra from both approaches were compared for residual fringing, S/N , and wavelength calibration. No noteworthy differences were present, and the CarPy pipeline was utilized for the remainder of the data reduction. Each reduced echelle order was carefully normalized using a third order spline with defined knot spacing. Normalized orders were stitched together to provide a single one-dimensional spectrum from 3800–9400 Å.

The white dwarf HR 6141 was observed in March 2011 as a telluric standard. The S/N ratio for HR 6141 exceeds that in any of our standard or program stars. Although the atmospheric conditions at Las Campanas Observatory are certain to change throughout the night and between observing runs, we are primarily using this spectra to identify lines that are affected by telluric absorption. However, critical transitions necessary for abundance analyses that are affected by the Earth’s atmosphere have been corrected for telluric absorption. The details of these corrections are discussed on a line-by-line basis.

3. ANALYSIS

3.1. Radial Velocities

The radial velocity for each star was determined in a two-step method. An initial estimate of the radial velocity was ascertained by cross-correlation with a synthetic spectrum of a giant star with $T_{\text{eff}} = 4500 \text{ K}$, $\log g = 1.5$, and $[M/H] = -1.0$ across the wavelength range 8450–8700 Å. The observed spectrum was shifted to the pseudo-rest frame using this initial velocity estimate. Velocities found from cross-correlation are typically within 1 km s^{-1} of our final published value.

With our spectra at near-rest, we measured the equivalent widths of ~ 200 lines by automatically fitting Gaussian functions to the absorption profiles (see Section

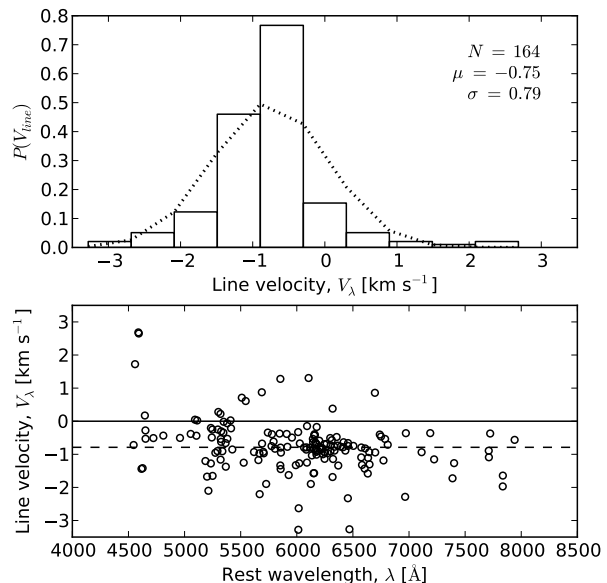


FIG. 1.— Residual velocities for each absorption line with a well-fitted Gaussian profile after correcting for doppler shift using the initial cross-correlation measurement. The mean residual velocity -0.75 km s^{-1} is within the $1\text{-}\sigma$ cross-correlation uncertainty of $\pm 0.9 \text{ km s}^{-1}$.

3.2). Fitted Gaussian profiles provide us with a measured equivalent width, the full-width half-maximum (FWHM) and the central wavelength of the profile. Thus, the residual radial velocity can be found from the ratio of the central and rest wavelengths. The final radial velocity for the star is provided by the initial velocity and the mean of ~ 200 residual line velocity measurements. Figure 1 shows the line velocities for HD 41667 after being placed at pseudo-rest using our cross-correlation velocity of 314.4 km s^{-1} . As expected, the mean residual offset is small (-0.75 km s^{-1}), and the standard deviation is 0.79 km s^{-1} from 164 line measurements. This provides us with a final measured radial velocity of $313.6 \pm 0.1 \text{ km s}^{-1}$. This process was performed for all observations. The radial velocities published in Table 1 are the final values from this two-step method. Heliocentric velocities agree quite well with those compiled by Williams et al. (2011) from the RAVE survey: the mean offset is $\langle \Delta V_{\text{hel}} \rangle = 2.5 \pm 2.7 \text{ km s}^{-1}$, demonstrating the accuracy of the velocities published in the RAVE catalog.

3.2. Line Measurements

For the measurement of atomic absorption lines, we employed the line list of Yong et al. (2005) with additional transitions of Cr, Sc, Zn, and Sr from Frebel et al. (2010). The line list was augmented with hyperfine-structure data for Sc and Mn from the Kurucz compilation ?. Molecular line data for CH was taken from ?. For lines with hyperfine structure, blended transitions or molecular features, we determined the abundance using a spectral synthesis approach. For all other transitions, equivalent widths were measured to determine the line abundance.

The equivalent widths for all absorption lines were measured automatically using software written for this study. Given the rest wavelength and an initial guess of

⁴ <http://code.obs.carnegiescience.edu/mike>

TABLE 1
OBSERVATIONS

Designation	α (J2000)	δ (J2000)	Observed Date	Airmass	Seeing (")	t_{exp} (secs)	S/N ^a (px ⁻¹)	V_{rad} (km s ⁻¹)	V_{hel} (km s ⁻¹)	V_{err} (km s ⁻¹)
Standard Stars										
HD 41667	06:05:03.7	-32:59:36.8	2011-03-13	1.005	1.0	90	340	313.6	297.1	0.1
HD 44007	06:18:48.6	-14:50:44.2	2011-03-13	1.033	1.0	120	280	-187.0	161.8	0.1
HD 76932	08:58:44.2	-16:07:54.2	2011-03-14	1.158	1.0	25	330	-132.6	117.8	0.1
HD 136316	15:22:17.2	-53:14:13.9	2011-03-14	1.118	0.9	...	400	59.8	-38.8	0.1
HD 141531	15:49:16.9	09:36:42.5	2011-03-14	1.309	0.9	...	350	17.7	2.8	0.1
HD 142948	16:00:01.6	-53:51:04.1	2011-03-14	1.107	1.0	...	320	5.3	29.9	0.1
Program Stars										
C2225316-14437	22:25:31.7	-14:54:39.6	2011-07-30	1.033	0.8	650	135	-168.6	-156.4	0.1
C2306265-085103	23:06:26.6	-08:51:04.8	2011-07-30	1.096	1.0	650	100	-240.4	-221.1	0.1
J221821-183424	22:18:21.2	-18:34:28.3	2011-07-30	1.026	0.9	650	115	-170.2	-159.5	0.1
J223504-152834	22:35:04.5	-15:28:34.9	2011-07-30	1.047	1.0	650	130	-179.0	-169.7	0.1
J223811-104126	22:38:11.6	-10:41:29.4	2011-07-30	1.218	1.2	650	115	-250.1	-235.7	0.1

^a S/N measured at 600 nm for each target.

the FWHM, a Gaussian profile is iteratively fitted to the absorption line. At the same time, the local continuum is found within 10 Å either side of the rest wavelength using a second-order polynomial. Measuring the local continuum ensures any errors in our initial normalisation or order-stitching do not propagate through to our equivalent width measurements. When determining the local continuum, any neighbouring group of pixels that deviate significantly ($>2\sigma$) from the local continua either belong to a persistent cosmic ray hit, or they are trough points of a neighbouring absorption profile. We attempt to fit a Gaussian profile to each group of deviating pixels, using the current best estimate for the local continuum. If a Gaussian profile is successfully fitted to the deviating group and its surrounding pixels, we assume the outlier points belong to an absorption line and all pixels belonging to that profile are excluded from the continuum determination.

When fitting Gaussian profiles, the χ^2 difference between the observed spectra and the fitted function is minimized. In order to account for crowded absorption regions, where the χ^2 value might be influenced by a nearby or blended profile, our χ^2 function is weighted based on the distance to the rest wavelength by the function

$$W_{\lambda_i} = 1 + \exp\left(\frac{-(\lambda_i - \lambda_r)^2}{4\sigma^2}\right) \quad (1)$$

where the rest wavelength (λ_r) and profile sigma⁵ (σ) are free parameters in the iterative fitting process. As a consequence of Eq. 1, pixels near the rest wavelength are weighted higher than those on the wings, forcing the fitting scheme to disregard blended or crowded surroundings. Although this approach relies on a reasonably accurate initial radial velocity correction of <4 km s⁻¹ – which is easily achieved – it greatly improves the accuracy and robustness of the equivalent width measurements.

The results of our iterative Gaussian fitting approach are *completely insensitive* to the initial FWHM guess.

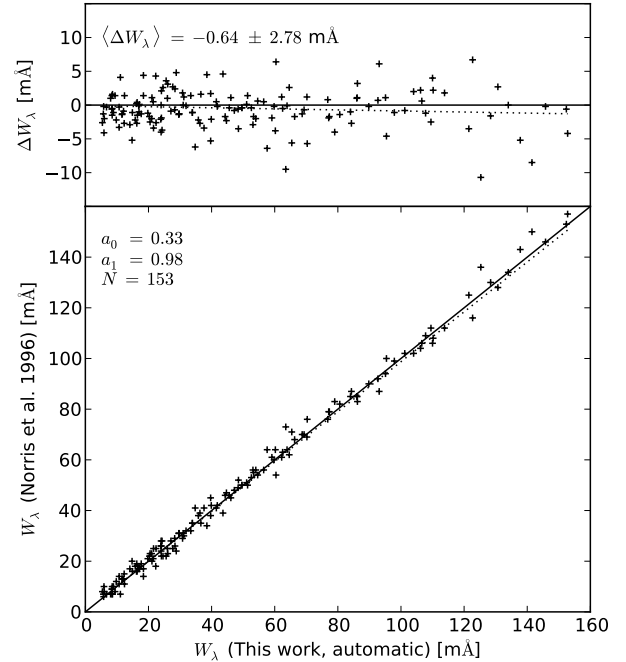
⁵ Recall $\text{FWHM} = 2\sigma\sqrt{2\log_e 2}$ 

FIG. 2.— A comparison showing equivalent widths measured for HD 140283 using our automatic routine (see §3.2), and those found by careful hand measurements in Norris et al. (1996). No systematic trend is present, and the mean difference between these studies is $\langle \Delta W_{\lambda} \rangle = -0.64 \pm 2.78$ mÅ.

Increasing the initial FWHM estimate from 0.1 Å to 1 or 2 Å – which are unphysically large values for high-resolution spectra – does not alter either the FWHM or the equivalent width for any of our measurements. Only a small increase in computational cost is observed. Although we are extremely confident in our equivalent width measurements, every absorption profile was examined by eye for quality, and spurious measurements were excluded.

We list the atomic data and measured equivalent

widths for transitions used during this analysis in Table ???. Saturated lines were excluded by removing measurements with reduced equivalent widths, $\log_{10}(EW/\lambda) > -4.5$ dex. A minimum detectable equivalent width was calculated as a function of wavelength based on the S/N , and only lines that exceeded a $3\text{-}\sigma$ detection significance were included. We have verified the approach by comparing our measurements of 156 lines in HD 140283 with the study of Norris et al. (1996). We only included measurements in the Norris et al. (1996) study that were not marked with questionable line quality parameters.

Excellent agreement is found between the two studies, which is illustrated in Figure 2. The mean difference is a negligible $-0.64 \pm 2.78 \text{ m}\text{\AA}$, and no systematic trend is present. We note that the scatter may be directly attributed to the observed S/N ratio, as other studies (Frebel et al. 2013, submitted) using the same equivalent width measurement software described here find better agreement with hand measurements for spectra with higher S/N ratios: $0.20 \pm 0.16 \text{ m}\text{\AA}$ with Aoki et al. (2007) and $0.25 \pm 0.28 \text{ m}\text{\AA}$ with Cayrel et al. (2004) for

TABLE 2
List of Line Transitions and Equivalent Width Measurements

Wavelength (Å)	Transition	χ (eV)	$\log gf$	Equivalent Widths				
				C2225316-14437 (mÅ)	C2306265-085103 (mÅ)	J221821-183424 (mÅ)	J223504-152834 (mÅ)	J223811-104126 (mÅ)
6300.300	8.0	0.00	-9.717	45.4	66.9	38.5	32.8	17.9
6363.780	8.0	0.02	-10.185	19.5	28.3	13.0	18.8	...
5688.190	11.0	2.11	-0.420	49.0	131.5	38.4
6154.230	11.0	2.10	-1.530	24.1	38.9	...	48.5	...
6160.750	11.0	2.10	-1.230	37.7	58.5	...	65.7	...
6318.720	12.0	5.11	-1.970	...	47.9	14.7	62.8	8.9
6319.240	12.0	5.11	-2.220	30.8	...	5.5
6965.410	12.0	5.75	-1.510	59.2	...
7387.690	12.0	5.75	-0.870	51.7	56.3	24.7	76.0	24.0
6696.020	13.0	3.14	-1.340	72.8	63.6	13.0
6698.670	13.0	3.14	-1.640	39.7	33.4	...	39.5	...
7835.310	13.0	4.02	-0.470	47.8	38.4	...	55.9	5.4
7836.130	13.0	4.02	-0.310	62.8	44.7	...	69.1	13.2
5690.430	14.0	4.93	-1.751	56.2	43.8	25.7	53.4	16.8
5793.070	14.0	4.93	-1.843	46.1	39.8	19.3	48.4	...
6125.020	14.0	5.61	-1.506	40.9	23.4	10.9	34.7	...
6145.010	14.0	5.62	-1.362	33.9	21.7	16.1	32.7	10.0
6155.130	14.0	5.62	-0.786	67.4	53.1	35.3	72.0	25.0
6166.440	20.0	2.52	-1.142	94.2	105.5	42.3	99.5	35.9
6169.040	20.0	2.52	-0.797	112.1	120.9	66.3	120.5	55.5
6169.560	20.0	2.53	-0.478	127.9	141.2	83.7	136.4	71.3
6455.600	20.0	2.52	-1.290	80.8	91.4	31.4	89.2	26.0
5526.820	21.1	1.77	0.130	98.8	113.3	100.8	98.4	51.1
5657.880	21.1	1.51	-0.500	96.5	107.5	92.7	95.4	41.2
5667.150	21.1	1.50	-1.240	59.4	75.0	45.0	58.5	14.5
5669.040	21.1	1.50	-1.120	...	92.5	57.3	75.2	18.2
6245.610	21.1	1.51	-0.980	67.1	83.6	53.3	67.4	14.8
6604.600	21.1	1.36	-1.480	65.6	82.1	49.4	65.9	17.8
6064.630	22.0	1.05	-1.888	59.7	80.9	...	58.6	...
6091.170	22.0	2.27	-0.367	45.2	59.1	...	56.3	...
6312.240	22.0	1.46	-1.496	46.2	63.4	...	48.8	...
6336.100	22.0	1.44	-1.687	35.9	54.1	...	42.3	...
5154.080	22.1	1.57	-1.920	112.2	...	114.0	...	53.9
5185.910	22.1	1.89	-1.350	...	101.4	105.5	...	55.3
5336.790	22.1	1.58	-1.690	116.3	124.6	119.5	104.0	61.4
5381.030	22.1	1.59	-2.080	...	131.4	101.9	109.9	48.0
5727.060	23.0	1.08	-0.010	122.4	...	26.0	116.8	9.1
6090.220	23.0	1.08	-0.060	93.6	115.6	23.6	92.8	...
6216.360	23.0	0.28	-1.290	108.8	...	16.9	109.3	...
6251.820	23.0	0.29	-1.340	94.7	124.4	...	92.4	...
6274.640	23.0	0.27	-1.670	65.5	93.8	...	61.5	...
6504.160	23.0	1.18	-1.230	22.9	33.7	...	31.9	...
4545.950	24.0	0.94	-1.370	80.2
4580.056	24.0	0.94	-1.650	44.2
4616.137	24.0	0.98	-1.190	128.7	139.3	89.4	126.2	59.9
4626.188	24.0	0.97	-1.320	122.2	136.4	82.2	...	56.9
4646.150	24.0	1.03	-0.740	110.6	146.1	75.3
4651.280	24.0	0.98	-1.460	127.8	140.6	75.4	116.3	48.4
4652.158	24.0	1.00	-1.030	138.5	...	96.9	138.0	66.7
5206.040	24.0	0.94	0.020	132.8
5247.564	24.0	0.96	-1.640	141.4	...	76.1	...	46.7
5296.690	24.0	0.98	-1.360	149.9	...	85.0	141.0	59.0
5300.740	24.0	0.98	-2.000	120.5	112.2	...
5345.800	24.0	1.00	-0.950	115.4	...	81.1
5348.310	24.0	1.00	-1.210	150.8	...	94.8	142.4	63.0
5409.770	24.0	1.03	-0.670	132.4	...	92.1
4558.594	24.1	4.07	-0.656	101.8	46.5
4588.142	24.1	4.07	-0.826	46.0	53.0	60.5	55.0	36.0

TABLE 2
List of Line Transitions and Equivalent Width Measurements

Wavelength (Å)	Transition	χ (eV)	$\log gf$	Equivalent Widths				
				C2225316-14437 (mÅ)	C2306265-085103 (mÅ)	J221821-183424 (mÅ)	J223504-152834 (mÅ)	J223811-104126 (mÅ)
4591.992	24.1	4.07	-1.419	29.1	28.5	19.6
6013.530	25.0	3.07	-0.251	89.2	114.6	22.2	109.4	14.8
6016.670	25.0	3.08	-0.100	94.0	116.0	28.1	113.0	17.1
6021.800	25.0	3.08	0.034	97.5	116.0	39.1	110.7	19.9
5044.210	26.0	2.85	-2.034	33.7
5054.640	26.0	3.64	-1.938	38.0
5242.490	26.0	3.63	-0.980	94.3	101.8	72.9	...	49.2
5321.110	26.0	4.43	-1.106	35.0	35.3	11.1
5322.040	26.0	2.28	-2.840	93.1	103.0	59.5	...	30.9
5326.140	26.0	3.57	-2.130	40.4	51.7	13.7	48.4	...
5365.400	26.0	3.57	-1.040	...	100.3	...	93.8	...
5367.480	26.0	4.41	0.430	108.4	118.0	92.4	119.1	73.7
5379.570	26.0	3.69	-1.530	71.4	81.4	34.9	75.6	19.6
5491.840	26.0	4.18	-2.250	17.3	...
5618.630	26.0	4.21	-1.292	43.5	54.3	20.2	57.4	11.3
5701.550	26.0	2.56	-2.216	118.5	134.8	91.8	119.5	49.5
5705.470	26.0	4.30	-1.420	29.2	41.5	10.9	44.5	7.7
5741.850	26.0	4.25	-1.689	36.2	37.0	13.0	48.2	...
5775.080	26.0	4.22	-1.310	55.0	62.1	25.3	67.4	14.7
5778.450	26.0	2.59	-3.480	42.8	55.8	13.4	50.1	...
5811.920	26.0	4.14	-2.430	10.9	...
5837.700	26.0	4.29	-2.340	12.9	...
5853.160	26.0	1.49	-5.280	30.4	43.4	6.3	34.7	...
5855.090	26.0	4.60	-1.547	13.3	20.3	...	22.8	...
5856.100	26.0	4.29	-1.640	27.9	40.2	...	42.7	...
5858.790	26.0	4.22	-2.260	...	11.4	...	16.9	...
5909.970	26.0	3.21	-2.640	56.0	72.6	18.5	63.3	...
5916.250	26.0	2.45	-2.994	92.9	105.1	51.2	95.4	17.7
5927.800	26.0	4.65	-1.090	32.4	36.7	12.2	50.9	...
5956.690	26.0	0.86	-4.608	121.7	143.8	70.3	107.8	25.5
6012.210	26.0	2.22	-4.070	44.4	58.8	11.5	53.0	...
6019.360	26.0	3.57	-3.360	7.0	11.3	...
6027.050	26.0	4.07	-1.106	66.2	77.0	36.2	77.2	23.5
6054.080	26.0	4.37	-2.310	5.6	8.1	...	12.9	...
6105.130	26.0	4.55	-2.050	...	10.9	...	14.8	...
6120.240	26.0	0.91	-5.970	35.2	52.7	8.5	32.4	...
6151.620	26.0	2.17	-3.299	88.9	102.9	46.9	87.0	18.2
6157.730	26.0	4.08	-1.320	...	81.2	33.2	78.1	18.8
6159.380	26.0	4.61	-1.970	...	9.6	...	13.6	...
6165.360	26.0	4.14	-1.490	40.6	51.6	14.2	54.0	10.8
6173.340	26.0	2.22	-2.880	109.6	125.6	70.7	105.6	34.9
6180.200	26.0	2.73	-2.637	86.2	100.6	44.3	91.5	20.8
6200.310	26.0	2.61	-2.437	105.2	122.2	70.8	105.4	36.6
6219.280	26.0	2.20	-2.433	134.3	153.3	103.3	127.4	56.7
6229.230	26.0	2.84	-2.846	60.1	73.1	21.0	65.8	13.6
6232.640	26.0	3.65	-1.283	92.6	104.3	58.3	103.0	35.6
6246.320	26.0	3.60	-0.894	114.0	129.2	90.5	124.1	61.7
6265.130	26.0	2.17	-2.550	132.9	155.0	94.8	129.7	55.5
6270.220	26.0	2.86	-2.500	76.7	93.6	41.2	79.1	17.4
6271.280	26.0	3.33	-2.728	31.6	44.9	13.4	43.6	...
6297.790	26.0	2.22	-2.740	119.3	...	81.3	111.3	42.3
6301.500	26.0	3.65	-0.766	115.0	130.6	91.1	117.9	...
6322.690	26.0	2.59	-2.426	111.0	124.4	74.2	103.5	41.6
6336.820	26.0	3.68	-0.916	106.6	116.8	81.2	113.6	52.8
6353.840	26.0	0.91	-6.477	11.8	23.7	...	14.1	...
6355.030	26.0	2.84	-2.403	...	122.2	58.9	...	27.8
6411.650	26.0	3.65	-0.734	122.5	135.1	97.8	131.8	68.2
6469.190	26.0	4.84	-0.770	18.7
6574.230	26.0	0.99	-5.004	84.1	118.5	35.4	87.0	...
6575.020	26.0	2.59	-2.727	100.7	118.2	55.5	103.4	23.4
6581.210	26.0	1.50	-4.705	72.4	87.5	21.7	69.6	...
6609.110	26.0	2.56	-2.692	102.0	118.8	60.9	103.1	29.1
6648.080	26.0	1.01	-5.918	37.1	54.9	...	37.9	...
6739.520	26.0	1.56	-4.820	43.1	60.8	...	44.5	...
6750.150	26.0	2.42	-2.621	110.9	128.9	78.6	109.5	40.2
6786.860	26.0	4.19	-1.850	22.5	29.1	...	32.3	...
6810.260	26.0	4.60	-1.000	36.2	46.9	14.5	54.9	8.5
6971.930	26.0	3.02	-3.390	21.0	30.3	...	28.7	...
7112.170	26.0	2.99	-3.044	45.4	59.3	13.3	53.0	...
7189.150	26.0	3.07	-2.796	57.5	66.3
7223.660	26.0	3.01	-2.269	87.2	114.4	47.2	90.8	...
7401.690	26.0	4.18	-1.660	38.9	50.5	14.7	59.7	...
7710.360	26.0	4.22	-1.129	62.5	76.7	32.5	75.4	...

TABLE 2
List of Line Transitions and Equivalent Width Measurements

Wavelength (Å)	Transition	χ (eV)	$\log gf$	Equivalent Widths				
				C2225316-14437 (mÅ)	C2306265-085103 (mÅ)	J221821-183424 (mÅ)	J223504-152834 (mÅ)	J223811-104126 (mÅ)
7723.200	26.0	2.28	-3.617	82.1	100.4	36.6	91.9	...
7941.090	26.0	3.27	-2.331	50.3	...	22.4	61.7	...
5234.620	26.1	3.22	-2.150	...	81.2	58.3
5325.550	26.1	3.22	-3.220	...	32.1	43.4	...	11.6
5414.070	26.1	3.22	-3.750	23.6	21.0	6.8
5425.260	26.1	3.20	-3.370	27.1	38.2	41.3	37.3	14.5
5991.380	26.1	3.15	-3.557	21.5	...	28.3	25.8	7.7
6084.110	26.1	3.20	-3.808	11.8	16.0	20.0	18.8	...
6149.260	26.1	3.89	-2.724	21.7	25.2	30.8	26.3	11.8
6247.560	26.1	3.89	-2.329	31.2	36.7	50.2	40.3	21.4
6369.460	26.1	2.89	-4.250	13.5	16.3	18.1	16.7	5.9
6416.920	26.1	3.89	-2.740	23.1	29.2	29.2	31.9	...
6432.680	26.1	2.89	-3.708	30.0	33.6	41.7	37.5	12.9
6456.380	26.1	3.90	-2.075	40.9	47.9	61.2	49.3	30.9
7224.490	26.1	3.89	-3.243	12.7	13.2	...
7711.720	26.1	3.90	-2.543	23.7	29.1	37.4	29.8	14.9
6189.000	27.0	1.71	-2.450	51.1	77.5	9.1	58.7	...
6455.030	27.0	3.63	-0.250	19.1	29.8	...	31.4	...
6632.450	27.0	2.28	-2.000	29.1	42.3	...	34.7	...
5846.990	28.0	1.68	-3.210	60.7	77.0	17.8	62.7	...
6086.280	28.0	4.26	-0.515	31.8	36.1	12.4	47.8	...
6175.370	28.0	4.09	-0.535	41.4	48.6	21.1	52.5	10.4
6177.240	28.0	1.83	-3.510	39.3	48.8	11.1	39.4	...
6204.600	28.0	4.09	-1.140	14.9	18.5	...	25.3	...
6635.120	28.0	4.42	-0.828	14.9	18.2	...	26.0	...
6772.320	28.0	3.66	-0.987	53.5	59.1	26.5	62.0	13.0
5105.540	29.0	1.39	-1.520	139.4	160.4	67.1	123.3	32.5
4722.150	30.0	4.03	-0.390	74.1	67.9	73.6	76.5	37.4
4810.528	30.0	4.08	-0.137	61.5	63.6	72.5	82.3	42.1
7800.290	37.0	0.00	0.130	60.9	...
5123.220	39.1	0.99	-0.830	16.5
5200.420	39.1	0.99	-0.570	100.9	...	65.8	78.6	26.5
5509.910	39.1	0.99	-1.010	103.0	94.4	47.0	95.4	15.7
5544.610	39.1	1.74	-1.080	29.9	18.8	9.5	16.2	...
6127.440	40.0	0.15	-1.060	56.3	44.9	...	29.7	...
6134.550	40.0	0.00	-1.280	49.6	38.7	...	23.6	...
6143.200	40.0	0.07	-1.100	54.4	44.6	...	30.7	...
5112.270	40.1	1.67	-0.590	21.8
5853.640	56.1	0.60	-1.010	143.5	121.4	110.8	99.8	49.6
6141.730	56.1	0.70	-0.080	213.6	177.6	166.4	151.1	93.1
5805.770	57.1	0.13	-1.560	47.7	28.8	13.0	25.1	...
6390.480	57.1	0.32	-1.410	43.0	22.0	11.6	18.6	...
5274.240	58.1	1.04	-0.320	29.1	...	12.7
5472.300	58.1	1.24	-0.180	19.4
4959.120	60.1	0.06	-0.800	79.9	74.0	35.0	64.2	...
5092.790	60.1	0.38	-0.610	47.3	...	21.9	20.9	...
5212.360	60.1	0.20	-0.960	61.4	61.9	19.6	51.6	...
5234.190	60.1	0.55	-0.510	71.9	57.9	17.9	47.3	...
5249.580	60.1	0.98	0.200	64.5	54.7	31.8	50.7	...
5255.510	60.1	0.20	-0.670	116.3	...	40.5
5293.160	60.1	0.82	0.100	74.2	71.6	29.0	62.5	...
5319.810	60.1	0.55	-0.140	86.6	...	34.4
6645.110	63.1	1.38	0.204	24.5	27.8	17.0	30.3	...

3.3. Model Atmospheres

We have employed the ATLAS9 plane-parallel stellar atmospheres of Castelli & Kurucz (2003). These one-dimensional models ignore any centre-to-limb spatial variations, assume hydrostatic equilibrium and no convective overshoot from the photosphere. The stellar parameter spacing between models is 250 K, 0.5 dex in surface gravity, 0.5 dex in $[M/H]$ and 0.1 dex in $[\alpha/Fe]$. We interpolated the temperature, gas and radiative pressure, electron density and opacities between atmosphere models using the Quickhull algorithm (Barber et al. 1996). Quickhull is reliant on Delaunay tessellation, which suffers from extremely skewed cells when the grid points vary in size by orders of magnitude – as T_{eff} values do

compared to $\log g$ or $[X/H]$. If unaccounted for, interpolating using such asymmetric cells can result in significant errors in atmospheric properties across all photospheric depths. We scaled each stellar parameter between zero and unity prior to interpolation in order to minimise these effects. During this step, $\log g$, $[M/H]$ and $[\alpha/Fe]$ values were scaled such that we simultaneously interpolate linearly in T_{eff} , $\log g$ and logarithmically in abundance ratios.

3.4. Stellar Parameters

The most recent version of the spectral synthesis code MOOG (Sneden 1973) has been used to derive individual line abundances and stellar parameters. This version

TABLE 3
STELLAR PARAMETERS

Designation	T_{eff} (K)	$\log g$ (dex)	v_t (km s ⁻¹)	[Fe/H] (dex)	T_{eff} (K)	$\log g$ (dex)	v_t (km s ⁻¹)	[Fe/H] (dex)	Source
Standard Stars									
HD 41667	4630	1.70	1.66	-1.21	4605	1.88	1.44	-1.16	Gratton et al. (2000)
HD 44007	4790	1.78	1.63	-1.80	4850	2.00	2.20	-1.71	Fulbright (2000)
HD 76932	5755	3.85	1.41	-1.06	5849	4.11	...	-0.88	Nissen et al. (2000)
HD 136316	4350	0.65	1.83	-1.92	4414	0.94	1.70	-1.90	Gratton & Sneden (1991)
HD 141531	4295	0.60	1.86	-1.74	4280	0.70	1.60	-1.68	Shetrone (1996)
HD 142948	4950	2.19	1.78	-0.79	4713	2.17	1.38	-0.77	Gratton et al. (2000)
Program Stars									
C2225316-14437	4325	1.26	1.78	-1.26	4235 ± 118	1.45 ± 0.21	1.96 ± 0.11	-1.20 ± 0.14	Wylie-de Boer et al. (2012)
C2306265-085103	4170	0.85	1.81	-1.17
J221821-183424	4590	0.90	1.91	-1.61	4395 ± 205	1.45 ± 0.35	1.96 ± 0.18	-1.15 ± 0.21	Wylie-de Boer et al. (2012)
J223504-152834	4590	2.15	1.45	-0.68	4597 ± 158	2.40 ± 0.14	1.47 ± 0.07	-0.98 ± 0.17	Wylie-de Boer et al. (2012)
J223811-104126	5140	2.96	1.33	-1.45	5646 ± 147	4.60 ± 0.15	1.09 ± 0.11	-1.20 ± 0.20	Wylie-de Boer et al. (2012)

employs Rayleigh scattering (Sobeck et al. 2011) instead of treating scattering as true absorption, which is particularly important for transitions blue-ward of 450 nm. This is noteworthy, but is less relevant for these analyses as most of our line measurements are red-ward of 450 nm. Absorption lines are assumed to form under the assumption of Local Thermal Equilibrium (LTE).

3.4.1. Effective Temperature

The effective temperature for each star was found by demanding a zero-trend in excitation potential and line abundance for each measured Fe I transition. In the same way, the microturbulence was found by demanding a zero trend in reduced equivalent width against abundance. Linear relationships with slopes of $|0.001|$ dex were considered to be converged.

3.4.2. Photometric Effective Temperatures

The effective temperatures published for all of our stars in Table ?? have been derived spectroscopically. As a consistency check for our spectroscopic temperatures, we have estimated effective temperatures using infrared photometry from the 2MASS catalog and empirical T_{eff} -color relationships. The $J - K$ color has been employed for these calculations because it has the least dependence on metallicity.

The Aquarius stream is relatively close and at high-latitude, so significant extinction caused by dust is not expected. The reddening maps of Schlegel et al. (1998) estimate that the extinction for our stars varies between $E(B-V) = 0.03$ to 0.07 mags. However, these maps are not perfect. As an alternative to using the Schlegel et al. (1998) dust maps, the level of extinction towards a star can be found by the strength of the interstellar Na D or K I lines (Munari & Zwitter 1997). The interstellar lines must be sufficiently separated from the stellar absorption lines in order for the extinction to be measurable. This was the case in only one of our stars, J223811. The equivalent width of the Na D1 line in J223811 is found to be $302.4 \text{ m}\text{\AA}$, corresponding to an $E(B-V) = 0.12^{+0.01}_{-0.02}$ according to the Munari & Zwitter (1997) relationship. This is a significantly higher value than the Schlegel et al. (1998) reddening map suggests: $E(B-V) = 0.07$. For

completeness, both extinction values have been used to calculate photometric temperatures.

Although all of our candidates are giant stars, two different T_{eff} -color relationships have been employed: the Alonso et al. (1999) calibration for giants, and the Casagrande et al. (2010) calibration for dwarfs and subgiants. All photometrically-derived temperatures are listed in 4. The Alonso et al. (1999) $J - K$ scale is insensitive to metallicity effects, and is in good agreement with our spectroscopic temperatures. For the Casagrande et al. (2010) $J - K$ relationship, which has a slight metallicity dependency, we have utilized the spectroscopically-derived [Fe/H] values shown in Table 3.

The effective temperatures found from spectroscopy agree fairly well with the photometric estimates. For three of our stars, the temperatures we find are in between the two color-temperature relationships. There are two noteworthy deviations: J223504-152834 and J223811-104126. For J223504-152834 we find the star to have an effective temperature of 4590 K, only 10 K hotter than the Casagrande et al. (2010) dwarf/subgiant relationship, yet ~ 500 K hotter than the Alonso et al. (1999) estimate. Our temperature of 4590 K is in good agreement with previous spectroscopic determinations (4795 K; Williams et al. (2011), 4597 K; Wylie-de Boer et al. (2012)). The fact that the Alonso et al. (1999) photometric temperature relationship for giants predicts a temperature that is ~ 500 K cooler than the spectroscopically-derived values may be attributed to an underestimated amount of dust towards J223504-152834. A higher than expected level of extinction along the line-of-sight would produce cooler photometric temperatures than the true effective temperature. An extinction of $E(B - V) = 0.10$ would be required for the Alonso et al. (1999) relation to yield a temperature of ~ 4500 K – within the uncertainties of our effective temperature derived from spectroscopy. Such a discrepancy in extinction is large, but not uncommon (e.g. see Peek & Graves 2010; Nataf et al. 2012). Although we suspect J223504-152834 to have a higher reddening than $E(B - V) = 0.04$, we have adopted the Schlegel et al. (1998) value for this analysis.

J223811-104126, the second temperature deviant, has two extinction values available: the Schlegel et al. (1998)

TABLE 4
REDDENING & PHOTOMETRIC TEMPERATURES

Designation	$E(B - V)$ (mag)	$(J - K)_0$	T_{phot}	
			Alonso (K)	Casagrande (K)
C222531-144370	0.03	0.75	4247	4391
C230626-085103	0.05	0.82	4091	4200
J221821-183424	0.03	0.64	4546	4747
J223504-152834	0.04	0.69	4110	4579
J223811-104126	0.07	0.48	5104	5367
	0.12 ^a	0.45	5215	5484

^aExtinction derived from interstellar Na D1 line (see 3.4.2)

value of $E(B - V) = 0.07$ and the 0.12 value determined from the interstellar Na D1 line. Given the inherent difficulties in producing dust maps, we believe the $E(B - V) = 0.12$ determination to be more accurate. However, using the Schlegel et al. (1998) extinction value with the Alonso et al. (1999) color-temperature relationship yields excellent agreement (5104 K) with our spectroscopic temperature of 5140 K. Employing our more accurate reddening determination yields 5215 K, still within the uncertainties of the relationship. The Casagrande et al. (2010) scale is ~ 250 K hotter in both cases.

With the exception of J223504-152834, the Alonso et al. (1999) giant relationship agrees well (± 100 K) with our spectroscopically-derived values. The Casagrande et al. (2010) relationship is also in relatively good agreement (most within 100 K, largest discrepancy is 220 K) with our spectroscopic temperatures, although we note that this relation was derived primarily for dwarfs/subgiants and our candidates are all giant stars.

3.4.3. Surface Gravity

The surface gravity for all stars was found by forcing the mean Fe I and Fe II abundances to be equal. The process is iterative: a zero trend with the excitation potential, reduced equivalent width and abundance must be maintained. For two stars, X and Y, the surface gravity could not be found by balancing the Fe I and II line abundances. The smallest difference between the median abundances was $\langle \text{Fe I} - \text{Fe II} \rangle = 0.05$ dex, which was considered to be converged. Varying the surface gravity from this solution did alter the mean Fe I and II abundances, but the difference $\langle \text{Fe I} - \text{Fe II} \rangle$ remained constant at 0.05 dex. In these two instances, the surface gravity was set to be closer towards the isochrone, while the $\langle \text{Fe I} - \text{Fe II} \rangle = 0.05$ dex condition was maintained.

3.4.4. Metallicity, $[M/H]$

The degeneracy between parameters required a refinement of the stellar parameters until the line abundances were consistent with the model atmosphere. After these parameters had converged, the model metallicity was exactly matched to that of our mean Fe I abundance. Line abundances that were unusually deviant ($> 3\sigma$) from the mean were removed. The largest number of outlier measurements removed for any observation was nine for C222531-144370, leaving 60 Fe I and 10 Fe II lines for analysis. The minimum number of Fe transitions used in any star was 44 lines (33 Fe I and 11 Fe II) for our hottest star, J223811-104126.

3.5. Abundances

We have scaled our abundances to solar values using the Sun's chemical composition described in Asplund et al. (2009).

3.5.1. Carbon

3.5.2. Oxygen

Oxygen is a particularly difficult element to measure. There are only a handful of lines available in an optical spectrum: the forbidden [O I] lines at 630 nm and 636 nm, and the O I triplet lines at 777 nm. The forbidden lines are very weak, and become immeasurable in either hot and/or metal-poor stars ($[\text{Fe}/\text{H}] \lesssim -1.5$ dex). When they are present, depending on the radial velocity of the star, the [O I] lines can be significantly affected by telluric absorption. Moreover, the 630 nm line is blended with a Ni I absorption line (Allende Prieto et al. 2001), and hence the region requires careful consideration. Although the O I triplet lines at 777 nm are stronger than the forbidden lines, they are extremely susceptible to non-LTE and 3D effects (Asplund & García Pérez 2001), and sensitive to changes in microturbulence.

The [O I] lines were measurable in four of our candidates. Careful consideration was taken when correcting for telluric absorption. The 6300 Å line in one of our candidates, C2306265-085103, was sufficiently affected by telluric absorption such that the line was considered immeasurable. Thus, only the 6363 Å transition was used to derive an oxygen abundance for C2306265-085103. In our hottest star, J223811-104126, the forbidden oxygen lines were not detected above a 3σ significance. After synthesising the region, we deduce a very conservative upper limit of $[\text{O}/\text{Fe}] < -0.50$ dex from the [O I] lines. This is consistent with the rest of our candidates, with [O/Fe] abundances varying between 0.41 to 0.57 dex.

In order to derive an oxygen measurement for J223811-104126, we were forced to use the triplet lines at 777 nm. Each line was synthesised, and a mean abundance was calculated for each candidate. Abundances determined from the oxygen triplet lines were systematically +0.27 dex higher than found from the [O I] lines. García Pérez et al. (2006) found [O/Fe] values based on the O I permitted triplet lines are on average $+0.19 \pm 0.07$ dex higher than those found from the forbidden lines, after non-LTE corrections of -0.08 dex had been applied to the permitted abundance. Thus, our 0.27 dex offset between measurements of the [O I] and O I triplet lines is exactly the same as found by García Pérez et al. (2006), which we attribute to a combination of systematic phenomena including non-LTE and 3D effects. García Pérez et al. (2006) concluded the weak forbidden lines, when not too weak, probably give the most reliable estimate of oxygen abundance.

From the permitted O I triplet, we derive an oxygen abundance of $[\text{O}/\text{Fe}] = 0.41 \pm 0.01$ dex (random scatter) for J223811-104126. This measurement will be systematically higher than the 'true' abundance if it were discernible from the [O I] lines, on the order of ~ 0.27 dex. When we apply this crude offset derived from the rest of our sample, we arrive at a corrected abundance of $[\text{O}/\text{Fe}] = 0.14 \pm 0.08$ dex for J223811-104126. This is the most oxygen-deficient star in our sample.

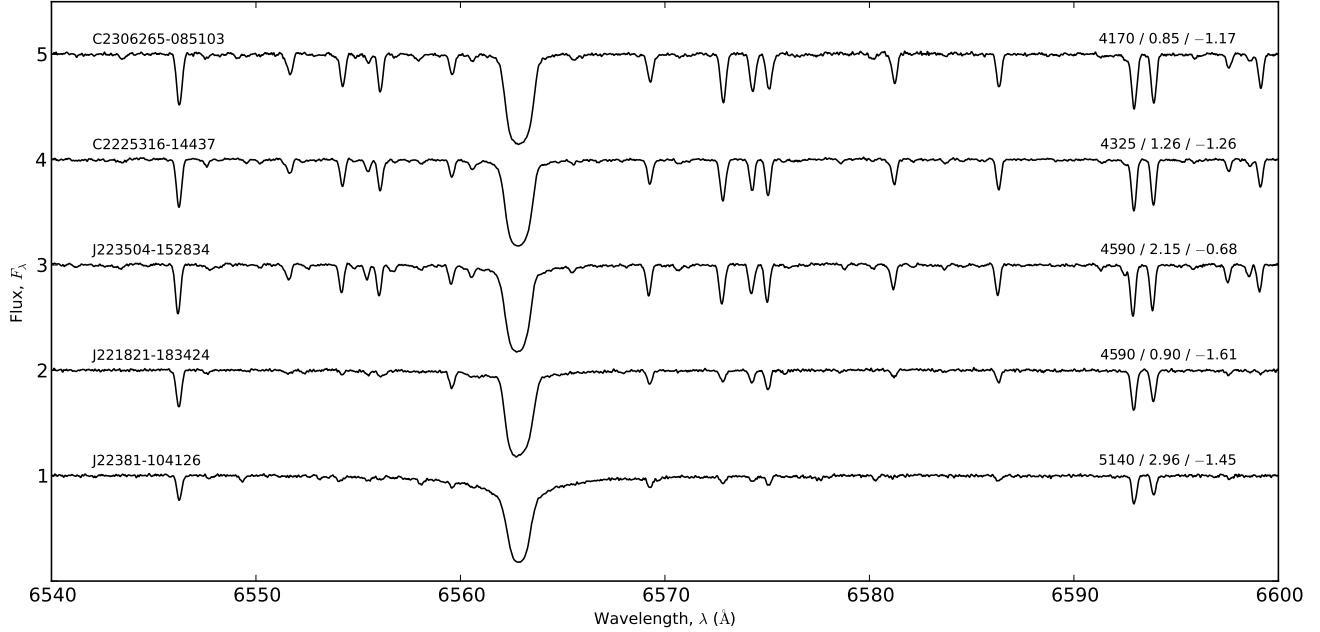


FIG. 3.— Sample spectra of the H- α region for all Aquarius stream candidates.

3.5.3. Sodium

Our line list includes three clean, unblended sodium lines at 5688Å, 6154Å and 6161Å. Not all three of these lines were detectable in each star. In the hottest and most metal-poor stars, J223811 and J221821-183424 respectively, only the 5688Å line was measurable. Consequently, an uncertainty of 0.10 dex was adopted for these stars. For stars where multiple sodium lines were available, the line-to-line scatter is reasonable: smaller than 0.09 dex.

3.5.4. α -elements (Mg, Ca, Si and Ti)

The α -elements (Mg, Ca, Si and Ti) are forged through α -particle capture in assorted burning stages of stellar evolution, including the burning of carbon, neon and silicon. Although Ti ($Z = 22$) is not formally an α -element, its abundance generally varies with those of the other α -elements and therefore has been included here.

Depending on the radial velocity of the star, some magnesium lines were be affected by telluric absorption, particularly the 6318Å and 6965Å transitions. Atmospheric absorption was most notable for C2225316-14437, where three of the four Mg transitions in our line list suffered some degree of telluric absorption, requiring an attentive correction. Every amended absorption profile was carefully examined, and lines with suspicious profiles were excluded from the final magnesium abundance.

Of all the α -elements, calcium has the smallest measurement scatter in our stars. Four line measurements were used for each star, with a measurement uncertainty of 0.01 dex. As shown in Figure ??, all Aquarius candidates show super-solar Ca abundances, ranging between 0.23 to 0.43 dex, consistent with both [Mg/Fe] and [Si/Fe] measurements.

However, C2225316-14437 has an unusually high silicon abundance ([Si/Fe] = 0.72), well outside the uncertainties of the rest of our sample. The silicon line

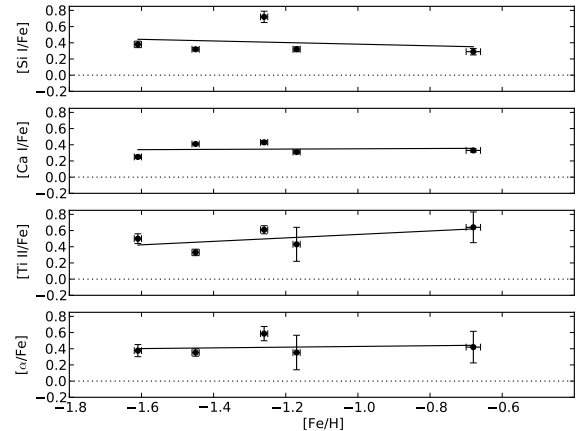


FIG. 4.— A plot showing $[\alpha/\text{Fe}]$ for all Aquarius stream stars.

abundances are in relatively good agreement with one another. If we exclude the most prominent outlier, then the mean abundance drops only slightly to $[\text{Si}/\text{Fe}] = 0.70 \pm 0.04$ dex. The lowest silicon line abundance for C2225316-14437 is $[\text{Si}/\text{Fe}] = 0.57$ dex, which is still significantly higher than the averaged abundance for any other star.

Titanium abundances for the stream stars are generally in agreement, showing typical α -enhancement signatures. Our titanium measurements are derived from clean, unblended lines. The number of transitions available in our spectra varies from four to seven. In our hottest and most metal-poor stars, no suitable Ti I transitions were available. In other stream candidates, the mean difference between species is $\langle \text{Ti I} - \text{Ti II} \rangle = 0.24$ dex. Although this discrepancy is not negligible, there are limited lines available for comparison, and our $\langle \text{Fe I} - \text{Fe II} \rangle$ abundances are in good agreement.

TABLE 5
STANDARD STAR ABUNDANCES

Species	N	$\log \epsilon(X)$	σ_ϵ	[X/H]	[X/Fe]	σ	Species	N	$\log \epsilon(X)$	σ_ϵ	[X/H]	[X/Fe]	σ
HD 41667							HD 44007						
O I	2	7.93	0.05	-0.76	0.45	0.04	O I	1	7.39	0.00	-1.30	0.50	0.00
Na I	3	4.87	0.16	-1.37	-0.16	0.09	Na I	2	4.42	0.08	-1.83	-0.03	0.06
Mg I	4	6.74	0.11	-0.86	0.35	0.05	Mg I	2	6.27	0.06	-1.33	0.47	0.04
Al I	4	5.12	0.11	-1.33	-0.12	0.06	Al I	1	4.76	0.00	-1.69	0.11	0.00
Si I	5	6.52	0.05	-0.99	0.22	0.02	Si I	5	6.06	0.07	-1.45	0.35	0.03
Ca I	4	5.46	0.06	-0.88	0.33	0.03	Ca I	4	4.92	0.02	-1.42	0.38	0.01
Sc II	6	2.12	0.13	-1.03	0.18	0.05	Sc II	6	1.38	0.10	-1.77	0.02	0.04
Ti I	4	3.96	0.04	-1.00	0.21	0.02	Ti I	1	3.46	0.00	-1.49	0.31	0.00
Ti II	3	4.12	0.25	-0.83	0.38	0.14	Ti II	4	3.52	0.15	-1.43	0.37	0.07
V I	6	2.88	0.13	-1.05	0.16	0.05	V I	4	2.16	0.03	-1.77	0.03	0.01
Cr I	10	4.25	0.09	-1.38	-0.17	0.03	Cr I	15	3.64	0.07	-2.00	-0.20	0.02
Cr II	3	4.54	0.25	-1.10	0.11	0.14	Cr II	3	3.97	0.02	-1.67	0.13	0.01
Mn I	3	3.94	0.01	-1.49	-0.28	0.01	Mn I	3	3.11	0.04	-2.32	-0.52	0.02
Fe I	61	6.29	0.12	-1.21	0.00	0.01	Fe I	51	5.70	0.13	-1.80	0.00	0.02
Fe II	13	6.28	0.06	-1.22	-0.01	0.02	Fe II	15	5.70	0.10	-1.80	0.00	0.02
Co I	3	3.75	0.11	-1.24	-0.03	0.06	Co I	0
Ni I	7	4.95	0.12	-1.27	-0.06	0.04	Ni I	4	4.43	0.04	-1.79	0.01	0.02
Cu I	1	2.76	0.00	-1.43	-0.22	0.00	Cu I	1	1.84	0.00	-2.35	-0.55	0.00
Zn I	2	3.33	0.08	-1.22	-0.01	0.06	Zn I	2	2.83	0.05	-1.73	0.07	0.04
Ba II	2	1.08	0.05	-1.10	0.10	0.03	Ba II	2	0.33	0.05	-1.85	-0.05	0.04
HD 76932							HD 136316						
O I	0	O I	1	7.20	0.00	-1.49	0.43	0.00
Na I	3	5.33	0.04	-0.91	0.15	0.02	Na I	2	4.15	0.03	-2.09	-0.17	0.02
Mg I	3	7.05	0.20	-0.55	0.51	0.12	Mg I	2	6.05	0.25	-1.54	0.38	0.17
Al I	4	5.44	0.06	-1.01	0.04	0.03	Al I	0
Si I	5	6.74	0.05	-0.77	0.29	0.02	Si I	4	5.86	0.05	-1.65	0.27	0.03
Ca I	4	5.57	0.02	-0.77	0.29	0.01	Ca I	4	4.69	0.02	-1.65	0.27	0.01
Sc I	0	Sc I	0
Sc II	6	2.23	0.11	-0.92	0.14	0.04	Sc II	5	1.32	0.05	-1.83	0.09	0.02
Ti I	1	4.35	0.00	-0.60	0.46	0.00	Ti I	3	3.23	0.03	-1.72	0.20	0.02
Ti II	3	4.34	0.03	-0.61	0.45	0.02	Ti II	4	3.52	0.14	-1.43	0.49	0.07
V I	3	3.15	0.13	-0.78	0.28	0.08	V I	5	1.88	0.06	-2.05	-0.13	0.03
Cr I	15	4.44	0.06	-1.20	-0.14	0.01	Cr I	12	3.52	0.05	-2.12	-0.20	0.02
Cr II	3	4.75	0.03	-0.89	0.17	0.02	Cr II	2	3.83	0.01	-1.81	0.11	0.00
Mn I	3	4.06	0.03	-1.37	-0.31	0.02	Mn I	3	3.09	0.02	-2.34	-0.42	0.01
Fe I	51	6.44	0.10	-1.06	0.00	0.01	Fe I	62	5.58	0.11	-1.92	0.00	0.01
Fe II	13	6.45	0.07	-1.05	0.01	0.02	Fe II	14	5.58	0.12	-1.92	0.00	0.03
Co I	0	Co I	3	3.15	0.06	-1.84	0.08	0.03
Ni I	5	5.27	0.02	-0.95	0.11	0.01	Ni I	5	4.23	0.10	-1.99	-0.07	0.04
Cu I	1	2.84	0.00	-1.35	-0.29	0.00	Cu I	1	1.75	0.00	-2.44	-0.52	0.00
Zn I	2	3.58	0.04	-0.97	0.08	0.02	Zn I	2	2.69	0.04	-1.87	0.05	0.02
Ba II	1	1.16	0.00	-1.02	0.04	0.00	Ba II	1	0.29	0.00	-1.89	0.03	0.00
HD 141531							HD 142948						
O I	2	7.29	0.01	-1.40	0.35	0.01	O I	2	8.39	0.03	-0.29	0.49	0.02
Na I	2	4.23	0.05	-2.01	-0.26	0.04	Na I	3	5.62	0.13	-0.62	0.16	0.07
Mg I	2	6.25	0.14	-1.35	0.40	0.10	Mg I	3	7.27	0.12	-0.33	0.45	0.07
Al I	2	4.69	0.10	-1.76	-0.02	0.07	Al I	4	5.88	0.08	-0.58	0.21	0.04
Si I	5	5.98	0.10	-1.53	0.22	0.04	Si I	5	7.02	0.05	-0.49	0.29	0.02
Ca I	4	4.84	0.02	-1.50	0.25	0.01	Ca I	4	5.75	0.01	-0.59	0.19	0.01
Sc II	4	1.50	0.04	-1.65	0.10	0.02	Sc II	6	2.59	0.11	-0.56	0.22	0.04
Ti I	4	3.30	0.07	-1.65	0.10	0.03	Ti I	4	4.42	0.09	-0.53	0.25	0.04
Ti II	4	3.69	0.08	-1.27	0.48	0.04	Ti II	3	4.40	0.21	-0.55	0.23	0.12
V I	5	2.06	0.08	-1.87	-0.12	0.04	V I	5	3.26	0.11	-0.67	0.11	0.05
Cr I	12	3.66	0.07	-1.98	-0.23	0.02	Cr I	13	4.69	0.15	-0.95	-0.17	0.04
Cr II	2	4.00	0.01	-1.63	0.11	0.01	Cr II	3	4.85	0.03	-0.79	-0.01	0.02
Mn I	3	3.21	0.04	-2.22	-0.47	0.02	Mn I	3	4.50	0.03	-0.93	-0.15	0.02
Fe I	54	5.75	0.06	-1.75	0.00	0.01	Fe I	61	6.72	0.10	-0.78	0.00	0.01
Fe II	13	5.78	0.04	-1.72	0.03	0.01	Fe II	13	6.69	0.06	-0.81	-0.03	0.02
Co I	3	3.26	0.07	-1.73	0.01	0.04	Co I	3	4.44	0.09	-0.55	0.23	0.05
Ni I	7	4.43	0.12	-1.79	-0.04	0.05	Ni I	5	5.61	0.05	-0.61	0.17	0.02
Cu I	1	1.99	0.00	-2.20	-0.46	0.00	Cu I	1	3.58	0.00	-0.61	0.17	0.00
Zn I	2	2.73	0.04	-1.83	-0.08	0.03	Zn I	2	3.91	0.05	-0.65	0.13	0.04
Ba II	1	0.43	0.00	-1.75	-0.01	0.00	Ba II	0

TABLE 6
PROGRAM STAR ABUNDANCES

Species	N	$\log \epsilon(X)$	σ_ϵ	[X/H]	[X/Fe]	σ	Species	N	$\log \epsilon(X)$	σ_ϵ	[X/H]	[X/Fe]	σ
J221821-183424							C2225316-14437						
O I	2	7.55	0.04	-1.13	0.47	0.02	O I	2	7.92	0.00	-0.77	0.49	0.00
Na I	1	4.71	0.00	-1.53	0.08	0.00	Na I	2	5.07	0.02	-1.17	0.09	0.01
Mg I	3	6.33	0.09	-1.27	0.34	0.05	Mg I	2	6.84	0.09	-0.76	0.50	0.06
Al I	1	5.05	0.00	-1.40	0.21	0.00	Al I	4	5.87	0.09	-0.58	0.68	0.04
Si I	5	6.28	0.08	-1.23	0.38	0.04	Si I	5	6.97	0.15	-0.54	0.72	0.07
Ca I	4	4.99	0.04	-1.35	0.25	0.02	Ca I	4	5.51	0.04	-0.83	0.43	0.02
Sc II	6	1.56	0.09	-1.59	0.01	0.04	Sc II	5	2.08	0.13	-1.07	0.19	0.06
Ti I	0	Ti I	4	4.04	0.02	-0.91	0.36	0.01
Ti II	4	3.85	0.13	-1.10	0.50	0.06	Ti II	2	4.29	0.08	-0.66	0.61	0.05
V I	3	2.26	0.01	-1.67	-0.06	0.01	V I	6	2.93	0.17	-1.00	0.26	0.07
Cr I	11	3.77	0.08	-1.87	-0.26	0.02	Cr I	8	4.29	0.16	-1.35	-0.08	0.06
Cr II	2	4.04	0.02	-1.60	0.00	0.02	Cr II	1	4.27	0.00	-1.37	-0.11	0.00
Mn I	3	3.30	0.03	-2.13	-0.52	0.02	Mn I	3	4.15	0.04	-1.28	-0.01	0.03
Fe I	52	5.89	0.09	-1.61	0.00	0.01	Fe I	60	6.24	0.10	-1.26	0.00	0.01
Fe II	13	5.91	0.05	-1.59	0.02	0.01	Fe II	10	6.19	0.06	-1.31	-0.05	0.02
Co I	1	3.38	0.00	-1.61	-0.00	0.00	Co I	3	3.92	0.12	-1.07	0.19	0.07
Ni I	5	4.62	0.14	-1.60	0.01	0.06	Ni I	7	5.05	0.09	-1.17	0.09	0.03
Cu I	1	2.16	0.00	-2.03	-0.42	0.00	Cu I	1	3.38	0.00	-0.81	0.45	0.00
Zn I	2	3.17	0.11	-1.39	0.22	0.08	Zn I	2	3.48	0.24	-1.08	0.19	0.17
Ba II	2	0.72	0.08	-1.47	0.14	0.05	Ba II	2	1.62	0.01	-0.56	0.70	0.00
J223504-152834							J223811-104126						
O I	2	8.46	0.10	-0.23	0.45	0.07	O I	1	8.26	0.00	-0.43	0.14 ^a	0.08
Na I	3	5.74	0.12	-0.50	0.18	0.07	Na I	1	4.86	0.00	-1.38	0.07	0.00
Mg I	3	7.41	0.15	-0.19	0.49	0.09	Mg I	2	6.47	0.02	-1.13	0.32	0.01
Al I	3	6.08	0.08	-0.37	0.31	0.05	Al I	2	5.10	0.14	-1.35	0.10	0.10
Si I	5	7.12	0.10	-0.39	0.29	0.04	Si I	3	6.38	0.04	-1.13	0.32	0.02
Ca I	4	6.00	0.03	-0.34	0.33	0.02	Ca I	4	5.30	0.03	-1.04	0.41	0.01
Sc II	6	2.70	0.14	-0.45	0.23	0.06	Sc II	6	1.75	0.14	-1.40	0.05	0.06
Ti I	4	4.59	0.02	-0.36	0.32	0.01	Ti I	0
Ti II	2	4.91	0.27	-0.04	0.64	0.19	Ti II	4	3.83	0.09	-1.12	0.33	0.04
V I	6	3.62	0.22	-0.31	0.37	0.09	V I	1	2.42	0.00	-1.51	-0.06	0.00
Cr I	7	4.88	0.09	-0.76	-0.08	0.04	Cr I	12	4.12	0.06	-1.52	-0.07	0.02
Cr II	3	4.83	0.50	-0.81	-0.13	0.29	Cr II	3	4.34	0.07	-1.30	0.15	0.04
Mn I	3	5.06	0.10	-0.37	0.31	0.06	Mn I	3	3.55	0.04	-1.88	-0.43	0.02
Fe I	63	6.82	0.12	-0.68	0.00	0.02	Fe I	33	6.05	0.06	-1.45	0.00	0.01
Fe II	12	6.82	0.07	-0.68	0.00	0.02	Fe II	11	6.00	0.09	-1.50	-0.05	0.03
Co I	3	4.50	0.13	-0.49	0.19	0.08	Co I	0
Ni I	7	5.61	0.09	-0.61	0.07	0.03	Ni I	2	4.82	0.04	-1.40	0.05	0.03
Cu I	1	3.82	0.00	-0.37	0.31	0.00	Cu I	1	2.39	0.00	-1.80	-0.35	0.00
Zn I	2	4.18	0.02	-0.38	0.30	0.02	Zn I	2	3.17	0.04	-1.39	0.06	0.03
Ba II	2	1.65	0.02	-0.53	0.15	0.01	Ba II	2	0.78	0.06	-1.40	0.05	0.04
C2306265-085103													
O I	2	7.96	0.02	-0.72	0.45	0.02							
Na I	2	5.25	0.00	-0.99	0.18	0.00							
Mg I	2	6.84	0.07	-0.76	0.41	0.05							
Al I	4	5.56	0.08	-0.89	0.28	0.04							
Si I	5	6.66	0.08	-0.85	0.32	0.03							
Ca I	4	5.48	0.04	-0.86	0.31	0.02							
Sc II	6	2.18	0.15	-0.97	0.20	0.06							
Ti I	4	4.06	0.03	-0.89	0.28	0.01							
Ti II	3	4.21	0.36	-0.74	0.43	0.21							
V I	4	2.88	0.06	-1.05	0.12	0.03							
Cr I	3	4.08	0.12	-1.56	-0.39	0.07							
Cr II	1	4.39	0.00	-1.25	-0.08	0.00							
Mn I	3	4.35	0.10	-1.08	0.09	0.06							
Fe I	62	6.33	0.12	-1.17	0.00	0.01							
Fe II	11	6.31	0.09	-1.19	-0.02	0.03							
Co I	3	4.00	0.15	-0.99	0.18	0.08							
Ni I	7	5.08	0.08	-1.14	0.03	0.03							
Cu I	1	3.55	0.00	-0.64	0.53	0.00							
Zn I	2	3.38	0.14	-1.18	-0.01	0.10							
Ba II	2	0.99	0.06	-1.19	-0.02	0.04							

^aAbundance derived from the permitted O I triplet instead of the forbidden [O I] lines, see §3.5.2

3.5.5. Aluminium

There are six aluminium transition lines available in our optical spectra. The strongest of these lines occur at 3944 and 3961 Å, and are visible in all of our stars. However, this is a particularly crowded spectral region: the lines fall between the strong Ca H and K lines, with the 3961 Å transition clearly in the wing of the Ca H line. This makes the continuum determination and subsequent aluminium measurement non-trivial, especially given the metallicity of our stars. Additionally, the 3944 and 3961 lines suffer from appreciable departures from LTE, resulting in under-estimated abundances by up to ~ 0.60 dex (Baumüller & Gehren 1997). Instead, we have measured Al abundances from other available transitions: the Al I lines at 6696, 6698, 7835 and 7836 Å. Although these lines are weaker than the bluer Al I lines, their surrounding regions are uncrowded from strong absorption lines.

Generally the four Al I lines are in reasonable agreement with one another, yielding random scatter of less than 0.05 dex. However, these lines were not always detected in the data. The strength of the lines is noticeably weakened below a $3\text{-}\sigma$ detection with decreasing metallicity and increasing temperature. For our most metal-poor star, J221821, only a single Al I line was detectable, and so we have adopted a conservative uncertainty of 0.10 dex.

3.5.6. Iron-peak Elements (Sc, V, Cr and Mn)

As expected, the Fe-peak elemental abundances exhibit similar trends (Figure 5). The noteworthy exception is chromium, where the median abundance is $[\text{Cr}/\text{Fe}] = -0.08 \pm 0.12$ and does not appear to vary with overall metallicity. The number of clean, suitable Cr I lines available between candidates fluxuated from three to twelve. Very little line-to-line scatter is present in both Cr I and II: the random scatter is below 0.04 dex for most stars, with the isolated example of J223504 where $\sigma([\text{Cr II}/\text{Fe}]) = 0.29$ dex, and only three lines were available. The Cr I and II abundances for J223504 are in good agreement (0.05 dex), and since none of the measured profiles were particularly unusual, we chose not to exclude outlier measurements. For all other stars, the Cr I – Cr II abundance differences varied between 0.02 dex up to 0.31 dex. The largest discrepancy occurred in our hottest star, where fewer chromium transitions were detected.

All other iron peak elements considered (Sc, V, Mn) all exhibit a slight downward trend in metallicity, with manganese demonstrating the most prominent gradient: varying between $[\text{Mn}/\text{Fe}] = -0.52$ dex to $+0.31$ dex in the most metal-poor and -rich stars respectively. The $[\text{Sc}/\text{Fe}]$ measurements presented in Figure 5 are calculated from six clean Sc II lines, and there is very minimal line-to-line scatter, the largest of which is 0.06 dex. Three Aquarius stream stars display $[\text{Sc}/\text{Fe}] \sim +0.20$, while J221821 and J223811 have $[\text{Sc}/\text{Fe}] = 0.01$ and 0.05 dex, respectively.

3.5.7. Nickel

Most Aquarius stream stars have seven clean Ni I transitions available. These lines are in excellent agreement, with typical scatter of 0.03 dex.

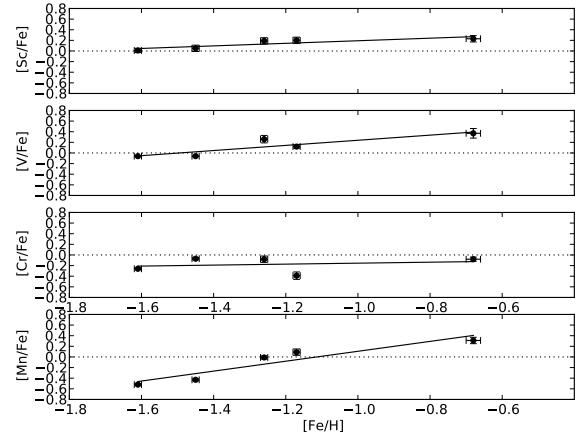


FIG. 5.— Iron peak elements for all stars.

3.5.8. Barium

Measuring barium requires some careful consideration. The strong resonance lines at 4554 Å and 4934 Å have appreciable hyperfine splitting, which can result in over-estimated abundances if unaccounted for. There are a few singly ionized lines available in our spectra that do not suffer from strong hyperfine splitting, namely the 5853, 6141 and 6496 Å transitions. Depending on the radial velocity of the star, sometimes our 6496 Å line was affected by small amounts of telluric absorption. In these cases the line was discarded. The abundances tabulated in Table 6 are based on the remaining clean Ba II lines at 5853 and 6141 Å, which are generally in good agreement with each other, and the 6496 Å line where available.

Our standard stars have $[\text{Ba}/\text{Fe}]$ abundances very typical of the Milky Way halo. Only one of our standard stars, HD 44007, has published $[\text{Ba}/\text{Fe}]$ abundances from high-resolution spectra. We find HD 44007 to have $[\text{Ba}/\text{Fe}] = -0.05 \pm 0.04$, which is at the mid-point of existing published measurements from Fulbright (2000) and Burris et al. (2000) of -0.27 and 0.05 dex, respectively.

With one exception, the Aquarius stream candidates have barium abundances that are quite similar to the stellar halo, ranging between $[\text{Ba}/\text{Fe}] = -0.02$ to 0.15 dex. The exception is C2225316, which has an anomalously high barium abundance of $[\text{Ba}/\text{Fe}] = 0.70$ dex. This is ~ 0.70 dex higher than the Milky Way trend at its given $[\text{Fe}/\text{H}] = -1.26$ dex. Our three Ba II lines in C2225316 are in excellent agreement: 0.67, 0.68, and 0.72 dex. The 6496 Å transition in C2225316 has a negligible telluric contribution and was included for this candidate. At least in Al, Si, Cr and Ba content (see sections ??, 3.5.4, ??), C225316 appears to be chemically distinct from the other Aquarius stream stars in our sample.

3.6. Distances

3.7. Dynamics

4. DISCUSSION

4.1. Stellar Parameter Discrepancies with Wylie-de Boer et al. (2012)

We seek to investigate the nature of the Aquarius stream, as well as the specific globular cluster origin

TABLE 7
OPTICAL PHOTOMETRY & ISOCHRONE DISTANCES

Designation	B (mag)	V (mag)	$(B - V)_0$ (mag)	Distance (kpc)
C222531-144370	13.75	12.52	1.20	...
C230626-085103	13.89	12.61	1.23	...
J221821-183424	13.08	12.13	0.92	...
J223504-152834	13.31	12.25	1.02	...
J223811-104126	12.69	11.93	0.73	...
	12.69	11.93	0.64 ^a	...

^aExtinction derived from interstellar Na D1 line (see SS3.4.2)

claim made by Wylie-de Boer et al. (2012). The stellar parameters reported in Wylie-de Boer et al. (2012) differ slightly to those published in Table 3. Wylie-de Boer et al. (2012) deduce their stellar parameters by minimizing the χ^2 difference between the observed spectra, and the Munari et al. (2005) synthetic spectral library after it was convolved and re-sampled to match the observations. The comparison regions used for analysis were 4900-5200 Å and 5575-5725 Å. In general, temperatures between the two studies agree within the uncertainties. The only aberration is J223811-104126, where we find an effective temperature of 5140 K, ~ 500 K cooler than the 5646 K found by Wylie-de Boer et al. (2012). Similarly, Williams et al. (2011) report a hotter effective temperature of 5502 K from low-resolution spectra. This is the largest discrepancy we see in any of our standard or program stars.

Photometric temperatures only lend marginal argumentative weight towards our spectroscopic temperatures. If the Schlegel et al. (1998) dust maps are employed, then the Alonso et al. (1999) and Casagrande et al. (2010) relations estimate the effective temperatures to be between 5104 K and 5367 K. Our spectroscopic temperature of 5110 K is in excellent agreement with the Alonso et al. (1999) prediction, but not in strong disagreement with the Casagrande et al. (2010) relation either. If we employ the reddening of $E(B - V) = 0.12$ that we have determined from interstellar Na D1 line, the photometric temperature increases slightly by ~ 100 K, still within the uncertainties of the Alonso et al. (1999) scale, but less so with the Casagrande et al. (2010) scale. We find the surface gravity for J223811-104126 to be 3.00 ± 0.50 , placing this star at the base of the red giant branch. Thus, if J223811-104126 is a giant star, our spectroscopic temperatures should be in slightly better agreement with the Alonso et al. (1999) scale, rather than the Casagrande et al. (2010) dwarf/sub-giant scale. However, Williams et al. (2011) and Wylie-de Boer et al. (2012) find this star to be a sub-giant, with a surface gravity $\log g = 4.16$ and 4.60 respectively. The Williams et al. (2011) and Wylie-de Boer et al. (2012) temperatures are 150 K and 300 K hotter than the Casagrande et al. (2010) prediction respectively. If our extinction value is employed, then the Williams et al. (2011) and Casagrande et al. (2010) temperatures are in good agreement, yet still 175 K cooler than the Wylie-de Boer et al. (2012) measurement.

As a test, we set the temperature for J223811-104126 to be 5600 K – within the temperature regime reported by Williams et al. (2011) and Wylie-de Boer et al. (2012). The slopes in abundance with excitation potential and

reduced equivalent width were large (#check smh: how many dex), and in doing so we could not find a physical solution for this temperature. Thus, although photometric temperatures do not help in solving this discrepancy, and the reddening measured from the interstellar Na D1 line may have made it worse, our high-resolution spectra indicates that J223811-104126 has an effective temperature of 5110 K and is indeed a giant star.

In the Wylie-de Boer et al. (2012) study, the surface gravity was determined during the χ^2 minimization process. Again, with the exception of J223811-104126, our surface gravities are largely in agreement. The only other noteworthy difference in surface gravity is for J221821-183424, where we find a lower gravity of $\log g = 0.80 \pm 0.30$ and Wylie-de Boer et al. (2012) find $\log g = 1.45 \pm 0.35 \text{ cm s}^{-2}$. Given the difference in S/N and resolution between these studies, this difference is not too concerning.

Wylie-de Boer et al. (2012) calculate microturbulence from empirical relationships derived by Reddy et al. (2003) for dwarfs and Fulbright (2000) for giants. These relationships are based upon the effective temperature and surface gravity. Our published microturbulent velocities agree excellently with the values presented in Wylie-de Boer et al. (2012), again with the exception of J223811-104126, where the difference in v_t can be directly attributed to the offsets in other observables.

Of all the stellar parameters (T_{eff} , $\log g$, v_t and $[\text{Fe}/\text{H}]$), the metallicities between our two studies vary the most. Here we discuss the potential causes for these discrepancies. In the Wylie-de Boer et al. (2012) study, after the stellar parameters (T_{eff} , $\log g$, v_t , and an initial $[\text{Fe}/\text{H}]$ estimate) had been determined through a χ^2 analysis, the authors synthesized individual Fe I and II lines using the MOOG code. Castelli & Kurucz (2003) stellar atmosphere models were employed – the same ones used in this study, albeit the interpolation schemes will have subtle differences. The median abundance of Fe I lines was taken as the overall stellar metallicity, scaled using the Grevesse & Sauval (1998) solar composition.

The study of Wylie-de Boer et al. (2012) is of slightly lower resolution ($\mathcal{R} = 25,000$ compared to $\mathcal{R} = 28,000$ presented here), but with a much lower S/N ratio: $\sim 25 \text{ pixel}^{-1}$ compared to $>100 \text{ pixel}^{-1}$ achieved here. Given the slightly lower spectral resolution and modest S/N in the Wylie-de Boer et al. (2012) study, there are fewer unblended absorption lines available. In fact, there are very few transitions present in their published line list: only 14 Fe I lines and 3 Fe II lines were available. For contrast, our metallicity determinations are usually based from ~ 50 Fe I and ~ 13 Fe II clean, unblended lines. Given the metallicity of these candidates and the spectral coverage (4120 to 6920 Å), it is somewhat surprising that there were not more transitions available to Wylie-de Boer et al. (2012).

The line list employed in the Wylie-de Boer et al. (2012) study contained fewer lines, and utilized different oscillator strengths than what we have used. The oscillator strengths in the Wylie-de Boer et al. (2012) study are astrophysical; they were derived from a reverse analysis from the Hinkle et al. (2003) solar atlas. Suspecting the differing line lists may be the cause of the metallicity discrepancy, we reanalysed our data using the Wylie-de

Boer et al. (2012) line list and stellar parameters. Indeed, we arrive at very similar metallicities to Wylie-de Boer et al. (2012). Without using their published stellar parameters a priori, in a ‘blind’ analysis employing just the Wylie-de Boer et al. (2012) line list, we also arrive at similar stellar parameters. However, given the limited number of lines available, subtle changes to the stellar parameters inflicted large changes to individual mean iron abundances. Additionally, we note that one Fe I transition at 6420.060 Å in the Wylie-de Boer et al. (2012) line list was not detected in any of our candidates at the 3- σ level, even though the S/N at this point exceeds 115 pixel⁻¹ in every observation. Thus, for this comparative analysis a maximum of 13 Fe I and 3 Fe II lines were available.

Given the line list employed in the Wylie-de Boer et al. (2012) study, the overall data quality and the lack of suitable iron lines available for analysis, it appears the Aquarius stream stars conspired to present a tight metallicity distribution function of $\sigma(\text{Fe}/\text{H}) = 0.10$ dex. When viewed in light of enhanced $[\text{Ni}/\text{Fe}]$, $[\text{Na}/\text{Fe}]$ abundance ratios, this chemistry is suggestive of a globular cluster origin. Our analysis of high-resolution spectra with high S/N reveals a much broader metallicity distribution for the stream. With just five stars we find the stream metallicity varies from $[\text{Fe}/\text{H}] = -0.65$ to -1.60 dex. Although this is a small sample, we find the calculated median abundance and standard deviation to be $[\text{Fe}/\text{H}] = -1.26 \pm 0.32$ dex.

4.2. The Aquarius Stream M.D.F.

Classical globular clusters typically exhibit very little chemical scatter. This is largely because they are primarily considered to be a single stellar populations, originating from a lone – largely homogenous – proto-stellar cloud. More recent observations have demonstrated shown that this is not always the case: many globular clusters clearly host multiple stellar populations. The separation between these populations is identifiable through chemical abundances, and often from photometry alone. In many cases, the chemistry between the two stellar populations are quite similar, still revealing minimal overall scatter within the cluster. There are some unusual exceptions to this rule, most notable of which is the globular cluster ω -Centauri (NGC 5139), which is seen to host many sub-populations with very different metallicity distributions. Without the explanation of multiple sub-populations in mind, the system would be seen to exhibit an unusually wide metallicity dispersion for a globular cluster.

Assuming all our candidates are stream members, we find a metallicity dispersion of $\sigma([\text{Fe}/\text{H}]) = 0.32$ dex. If the stream is the result of a disrupted system, this metallicity dispersion provides little indication on the progenitor. If the dispersion was smaller, confirming the observations of Wylie-de Boer et al. (2012), a globular cluster scenario is more likely. However, given the multiple stellar populations present in many globular clusters, which can exhibit total cluster dispersions up to X dex (NGC X), Y dex (NGC Y), our dispersion of 0.32 dex is somewhat inconvenient. Since dSph galaxies do not undergo chemical self-enrichment in the same way globular clusters do, they can exhibit significant metallicity disper-

sions – well over a dex, depending on the dwarf total luminosity. On its own, the metallicity of our stream stars does not provide any indication on the cause of the Aquarius stream, or its enrichment environment.

4.3. The Na-O Relationship

Extensive studies looking at stars in globular clusters have revealed variations in light-element abundances, most notably an anti-correlation in sodium and oxygen content Norris & Da Costa (1995); Carretta et al. (2009, and references therein). This chemical pattern has been repeatedly demonstrated in every well-studied globular cluster, although the strength of the anti-correlation varies in each system. Between generations of stars within a globular cluster, oxygen is converted into nitrogen, reducing the overall oxygen abundance. Even though oxygen undergoes internal mixing during its evolution along the giant branch, the detection of this chemical pattern in unevolved stars has led to the conclusion that observed abundance variations due to mixing are limited to Li, C, and N. Therefore, the light element anti-correlation required a different astrophysical explanation.

Sodium is primarily produced through carbon burning in massive stars by the dominant $^{12}\text{C}(^{12}\text{C}, p)^{23}\text{Na}$ process. The final Na abundance is dependent on the neutron excess of the star, which slowly increases during carbon burning due to weak interactions (?). Massive stars ($> 8M_{\odot}$) eventually deliver their manufactured sodium to the interstellar-medium through Sn II events. Because the eventual Sn II explosion is devoid of any significant beta-decay processes, the neutron excess of the exploded material is representative of the pre-explosion abundance.

The explosive material eventually condenses to form the next generation of stars, which will have a net increase in their neutron excess with respect to when their predecessors formed. Since the Na-production rate is correlated with the neutron excess, an overall increase in the total Na and Na-production rate between stellar generations is expected. Thus, an increase in the Na abundance between generations of massive stars is a natural consequence of nucleosynthesis. Sodium content also becomes important for production of Ni during the Sn II event (see §??) because ^{23}Na is the only stable isotope produced in significant quantities during the C- (or O-) burning stages. A small fraction of ^{22}Na is also forged through proton capture on ^{21}Ne in the carbon shell, an effect which is enhanced by neutrinos spallating abundant elements like ^{16}O and ^{20}Ne , making free protons available for capture (Woosley & Weaver 1995).

Oxygen depletion is likely the result of complete CNO burning within the stellar interior. The nucleosynthetic pathways that generate the Na-O anti-correlation are well known. However, the temperatures required to produce these patterns are not expected within the interiors of globular cluster stars. While the exact site for which these conditions occur remains under investigation, we can describe the abundance variation as a simple oxygen depletion (or dilution) model with time. Through comparisons with existing globular clusters, we can still draw inferences on the star-formation history of a system from measuring sodium and oxygen in a sample of its stars.

Carretta et al. (2009) defined three components of stars

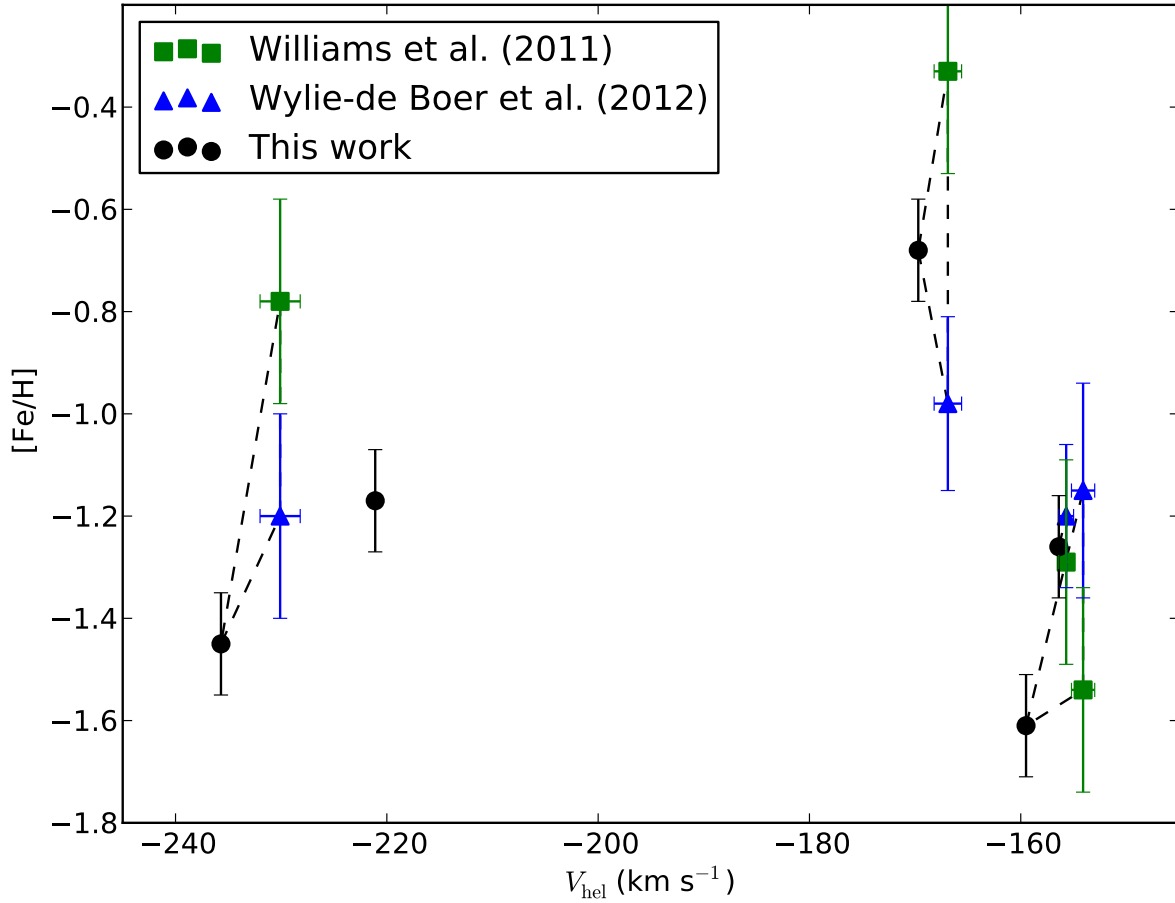


FIG. 6.— Heliocentric velocities and metallicities for Aquarius candidates in this sample. The measurements found by Williams et al. (2011) (green squares) and Wylie-de Boer et al. (2012) (blue triangles) are shown, and stars are linked by dashed lines. Wylie-de Boer et al. (2012) used the Williams et al. (2011) velocities, which is why their measurements are coincident on the abscissa.

exhibiting an inverse Na-O correlation within a population: primordial, intermediate, and extreme components. The $[\text{Na}/\text{Fe}]$ and $[\text{O}/\text{Fe}]$ abundances for a given star define which component it belongs to. Primordial (first-generation) stars are those with sodium and oxygen abundances which are similar to field stars of the same metallicity. For a well-studied system, stars with the lowest cluster $[\text{Na}/\text{Fe}]$ abundances are characterised as primordial. An intermediate component – the second-generation of stars – will have super-solar sodium abundances, and demonstrate a slight depletion in oxygen content. The oxygen exhaustion rate is ultimately dependent on the star-formation history of the cluster environment. The intermediate population is subdivided based on how much the sodium and oxygen abundances depart from the primordial population: stars with $[\text{O}/\text{Na}] > -0.9$ dex are classified as belonging to an extreme component of this Na-O pattern because they differ greatly from the primordial cluster abundance. The extreme O-depletion component has only been observed in a few clusters (preferentially more massive clusters with extended horizontal branches), indicating an long-lasting star-formation history in more massive clusters.

It is clear that careful consideration must be given

when inferring star-formation histories from observed stellar abundances. In addition to the normal care afforded for measuring elemental abundances from high-resolution spectroscopic data, attention must be given to telluric absorption, contamination from nickel transitions, as well as non-LTE and 3D effects when calculating oxygen abundances. Furthermore, when characterising the oxygen depletion rate – the strength of the Na-O anti-correlation in a given cluster – it is vital to sample stars belonging to all three components, where possible. If only a primordial sample of stars in a globular cluster is observed, their $[\text{Na}/\text{Fe}]$ and $[\text{O}/\text{Fe}]$ abundances will be indistinguishable from halo stars of a similar metallicity. In such a scenario, any inferred anti-correlation could equally be explained by intrinsic chemical scatter or observational uncertainties.

Wylie-de Boer et al. (2012) measured $[\text{Na}/\text{Fe}]$ and $[\text{O}/\text{Fe}]$ abundances for four of their six Aquarius stream members. This research has four stars in common with the Wylie-de Boer et al. (2012) study, but sodium and oxygen measurements exist for only three stars intersecting both samples, as the data quality for J223811-104126 in the Wylie-de Boer et al. (2012) study prohibited measuring oxygen. We have measurements for all of

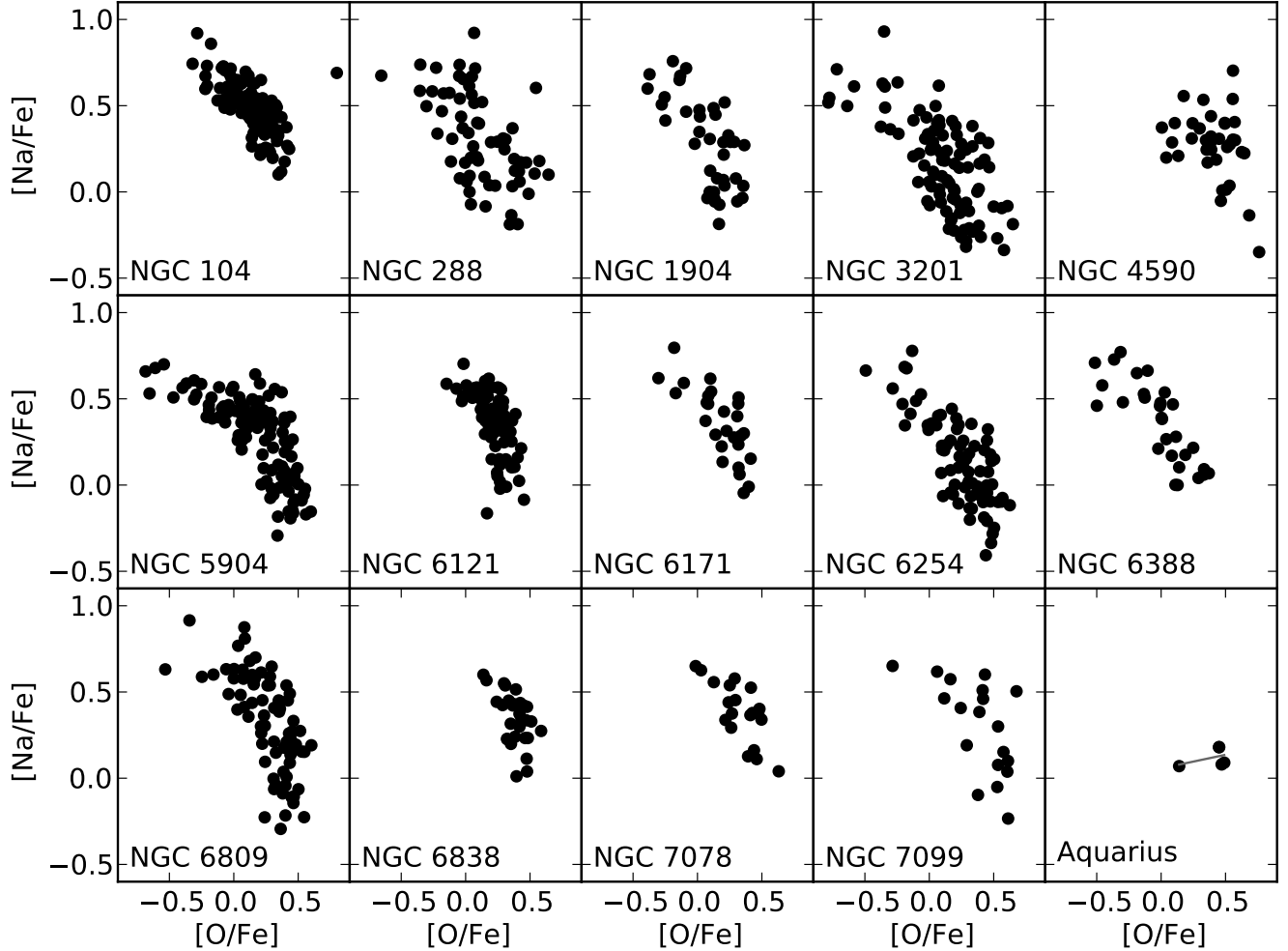


FIG. 7.— Oxygen and sodium abundances for 14 classical globular clusters from ?, demonstrating the clear inverse Na-O correlation, which is ubiquitous in all well-studied globular clusters. The $[O/Fe]$ and $[Na/Fe]$ abundances for the five Aquarius stream candidates are also shown (last panel).

our stars, including J223811-104126, for which we ascertained an upper limit from the $[O\ I]$ lines of $[O/Fe] < 0.5$ dex, and an inferred abundance of $[O/Fe] = 0.14 \pm 0.08$ from the $O\ I$ triplet lines. In Figure 8 we have plotted these abundances, including the corrected value for J223811-104126 rather than an upper limit.

The Wylie-de Boer et al. (2012) measurements indicate two stars with solar levels of Na – identical to field star Na abundances for their metallicity – and two stars with super-solar sodium content: J223504 and J232619. We also find J223504 to be sodium-enhanced with $[Na/Fe] = 0.18$, slightly lower than the Wylie-de Boer et al. (2012) value of 0.28 ± 0.21 dex. This discrepancy in $[Na/Fe]$ is the largest difference between the two studies, and still within the uncertainties published by Wylie-de Boer et al. (2012). The second star in their study with elevated sodium, J232619, is not in our sample. We find the additional star not present in the Wylie-de Boer et al. (2012) sample, C2306265, to be sodium enhanced to the same level of J223504 with $[Na/Fe] = 0.18$ dex.

The sodium-enhanced stars exhibit no depletion of oxygen; their chemistry does not demonstrate a classical Na-O anti-correlation. In fact, they have a slight positive relationship: the Na-enhanced stars in the Wylie-de Boer

et al. (2012) study show an increased oxygen content (within the uncertainties), contrary to an expected oxygen depletion between stellar generations within a globular cluster. With our revised oxygen abundances and two sodium-enhanced stars, we find a very slight positive relationship of $X.XX \pm X.XX$, and no evidence of a Na-O anti-correlation in the Aquarius stream.

If the Aquarius stream is the result of a disrupted globular cluster, a large part of the picture would still be missing. Most of the Aquarius stream stars studied to date (either in this sample or the Wylie-de Boer et al. (2012) study), would be classified as belonging to a ‘primordial’ component, with chemistry indistinguishable from the halo. Identifying more Aquarius stream members belonging to the intermediate component with strong oxygen depletion, or perhaps members of an extreme component, would be strong evidence for a Na-O anti-correlation and perhaps a globular cluster origin. Three stream stars identified to date (including two from this sample) could plausibly be classified as members of an intermediate population, with only a slight enhancement in sodium and no oxygen-depletion. Thus, if the strength of any Na-O relationship is to be used to vet potential disrupted hosts for the Aquarius stream, many

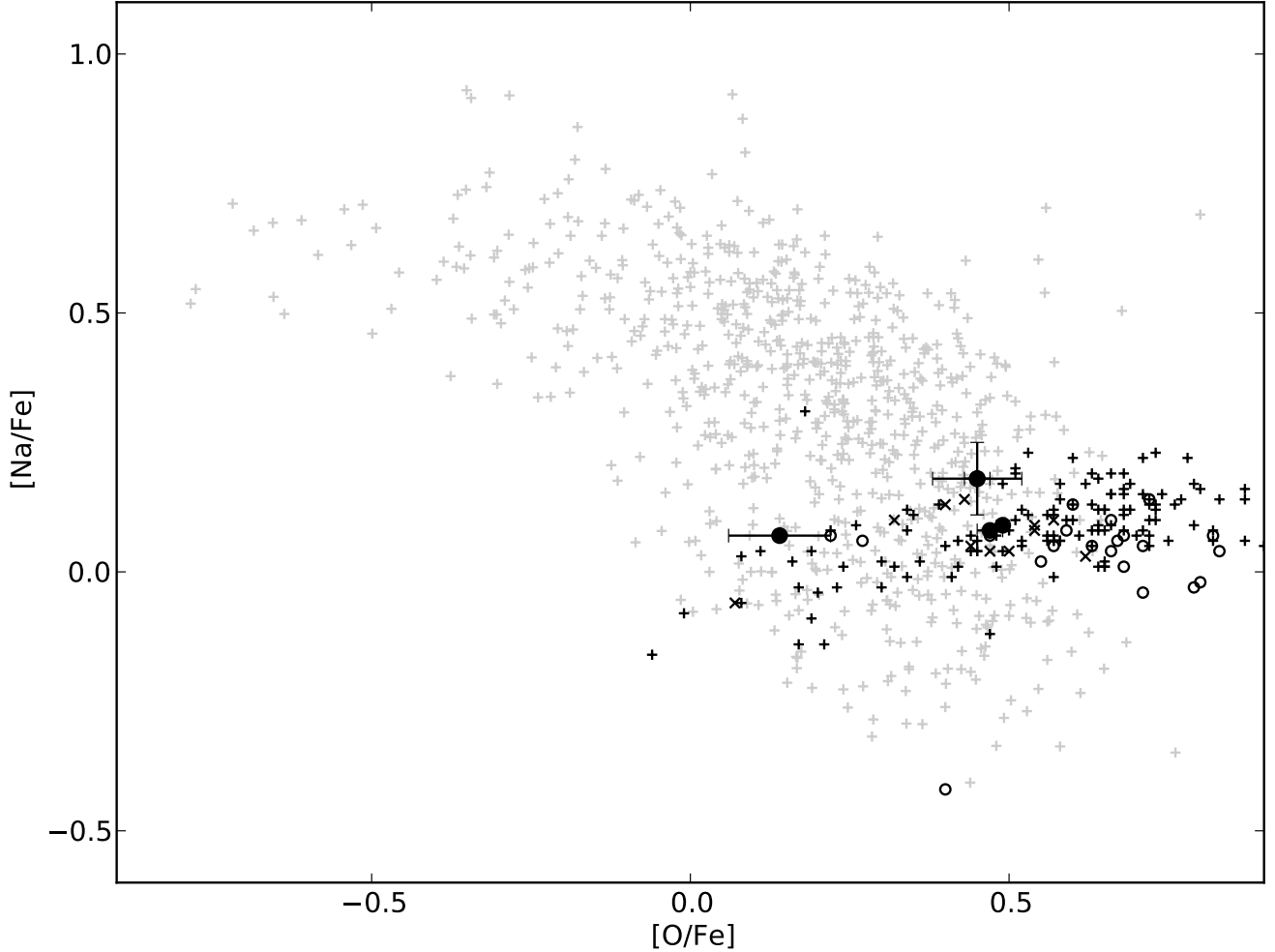


FIG. 8.— Oxygen and sodium abundances for thick disc (+), thin disc (x) and halo (o) stars from ?, and globular cluster stars from ? (grey symbols). The Aquarius candidate abundances are also shown (•), illustrating how their $[O/Fe]$, $[Na/Fe]$ content is not dissimilar from galactic stars. Ambiguous thick disc/thin disc stars in ? are marked with thick disc symbols (+), as are uncertain thick disc/halo stars with halo symbols (o).

more stream candidates will need to be identified, and observed with high-resolution and high S/N .

4.4. The Al-Mg Relationship

An inverse relationship between sodium and oxygen is not the only chemical pattern commonly observed in globular clusters. Although not ubiquitous to every system, many clusters exhibit an anti-correlation between aluminium and magnesium abundances. This is perhaps unsurprising, given the nucleosynthetic pathways for aluminium and magnesium. In addition to the CNO cycle operating during hydrogen burning, the Mg-Al chain can also operate under extreme temperatures ($T_6 \sim 3$ K; Arnould et al. 1999). Aluminium is produced by proton capture of magnesium, beginning with ^{24}Mg to ^{25}Al . The lifetime of β -decay to proton capture allows for the production of unstable ^{27}Si through proton capture. Seconds later, the isotope decays to ^{27}Al , completing the ^{27}Si path of the Mg-Al cycle. The alternative process from ^{25}Al involves proton capture to ^{26}Mg , but this process requires much higher temperatures ($T_6 \sim 7$ K). In fact, although the process operates from temperatures above 30 million K, large Mg-Al abundance variations are not

appreciable unless the temperatures reach $T_6 \sim 6.5$ K.

The Mg-Al cycle can explain the observed anti-correlation observed in some globular clusters, and most theoretical models predict such a pattern (#get citations from Amanda). However, the locations where these extreme temperatures can be found are under some debate. Theoretical models indicate that the interiors of globular cluster stars do not reach sufficient temperatures for the Mg-Al cycle to produce the observed variations. Thus, although the processes for creating these chemical patterns are understood, the exact site and requisite conditions are lacking a full description.

No inverse correlation has been observed in the Aquarius stream stars to date. Given that we do not find a Na-O anti-correlation, it is not surprising that a Mg-Al pattern has also not been observed. Wylie-de Boer et al. (2012) published magnesium and aluminium abundances for five stars in their Aquarius stream sample. No inverse correlation is present, and their abundances are not dissimilar from galactic stars. The abundances tabulated in Table ?? vary slightly with those presented in the Wylie-de Boer et al. (2012) sample. Two candidates are in good agreement: J221821 and J223811, albeit the

data quality in the Wylie-de Boer et al. (2012) study did not permit measuring aluminium for J223811. The other two stars common between studies are C2225316 and J223504, which we found to be the most abundant in both magnesium and aluminium.

While Wylie-de Boer et al. (2012) find almost no scatter (± 0.02 dex) in $[\text{Mg}/\text{Fe}]$ for stars common to both studies, we find C2225316 and J223504 to be almost $+0.20$ dex higher than the rest of the sample. The reason for this discrepancy is not obvious, given the stellar parameters between the two studies agree well, with the previously discussed exception of metallicity. In particular, the stellar parameters agree excellently for J223504, but we find $[\text{Fe}/\text{H}] = -0.68$ instead of the -0.98 as found by Wylie-de Boer et al. (2012). Of the Mg I profiles measured, only two transitions are common to both line lists: 6318Å and 6319Å. The oscillator strengths differ between studies; in these two lines the $\log gf$ differs by -0.24 and -0.27 dex respectively (our oscillator strengths are lower). This discrepancy only complicates the matter further, since if all other things being equal, then our abundances ought to be lower than the Wylie-de Boer et al. (2012) study.

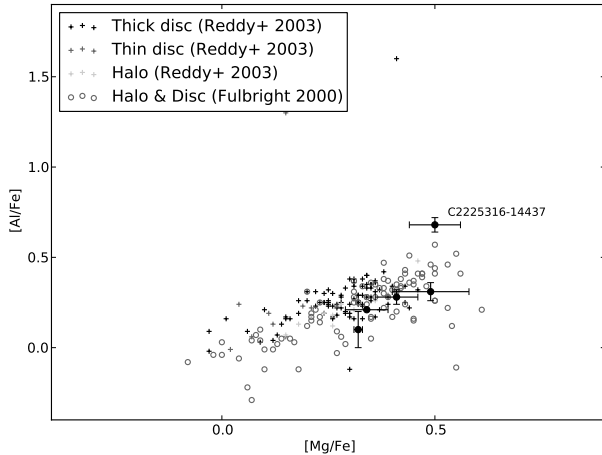


FIG. 9.— Magnesium and aluminium abundances for Aquarius candidates, and Milky Way halo/disc stars from Reddy et al. (2003) (+) and Fulbright (2000) (o). The chemically peculiar star, C2225316-14437, is marked.

The $[\text{Mg}/\text{Fe}]$ and $[\text{Al}/\text{Fe}]$ abundances found for the five Aquarius stars in this sample are illustrated in Figure 10. Interestingly, our stars exhibit a strong positive relationship, with a best-fitting slope of $[\text{Al}/\text{Fe}] = 2.15x[\text{Mg}/\text{Fe}] - 0.57$ ($R = \text{Y.YY}$). If we exclude C2225316, our chemically peculiar star with enhanced $[\text{Al}/\text{Fe}]$ relative to the rest of the sample, the slope decreases to $[\text{Al}/\text{Fe}] = 1.07x[\text{Mg}/\text{Fe}] - 0.19$ and the correlation coefficient R increases to Z.ZZ. Even when a Mg-Al anti-correlation is not detected in globular clusters, there is generally some scatter in $[\text{Al}/\text{Fe}]$ at constant $[\text{Mg}/\text{Fe}]$?. Few classical globular clusters exhibit a positive correlation.

A positive relationship between magnesium and aluminium can result from SN II contributions to the local interstellar medium. High-resolution observations of disc stars illustrate this correlation (?), demonstrating efficient SN II mixing. Some intermediate-mass ($4M_{\odot}$) AGB

models can also predict a positive correlation between aluminium and magnesium. Under extreme temperatures ($T_6 \sim 300$ K), substantial ^{25}Mg and ^{26}Mg are produced by α -capture onto ^{22}Ne by the $^{22}\text{Ne}(\alpha, n)^{25}\text{Mg}$ and $^{22}\text{Ne}(\alpha, \gamma)^{26}\text{Mg}$ reactions respectively. Following deep dredge up, significant ^{25}Mg and ^{26}Mg is mixed into the photosphere, more than the quantity of ^{26}Al produced through the Mg-Al cycle. This dredge up process replenishes the Mg which is expended during the Mg-Al pathway. Therefore, a positive relationship between magnesium and aluminium can occur if there has been significant contributions from intermediate mass AGB stars undergoing dredge up.

An unrealistically high fraction of intermediate-mass AGB stars would be required to produce the same chemical signature of a single SN II event. Given the efficiency of chemical pollution following supernovae, the observed correlation in the thick disc is likely the result of SN II events. However, since the chemical enrichment environment of the Aquarius stream is unknown, we cannot exclude either possibility. Distinguishing between these processes observationally requires careful measurements of magnesium isotope abundances ^{24}Mg (indicating supernovae mixing), ^{25}Mg and ^{26}Mg (suggesting significant AGB contribution), which is not possible given our S/N or spectral resolution.

4.5. The Na-Ni Relationship

Detailed chemical studies of nearby disk stars have noted a correlation with $[\text{Na}/\text{Fe}]$ and $[\text{Ni}/\text{Fe}]$ abundances. This relationship was first hinted in Nissen & Schuster (1997), where the authors found eight stars that were underabundant in $[\alpha/\text{Fe}]$, $[\text{Na}/\text{Fe}]$ and $[\text{Ni}/\text{Fe}]$. Interestingly, the authors noted that stars at larger galactocentric radii were most deficient in these elements. Fulbright (2000) saw a similar signature: stars with low $[\text{Na}/\text{Fe}]$ were only found at large ($R_{\odot} > 20$ kpc) distances. Nissen & Schuster (1997) proposed that since the outer halo is thought to have been built up by the accretion of dwarf satellite galaxies, then the Na-Ni pattern may be a chemical indicator of merger history within the galaxy.

With additional data from Nissen & Schuster (2011), the Na-Ni relationship was found to be slightly steeper than originally put forward. The pattern exists only for stars with $-1.5 < [\text{Fe}/\text{H}] < -0.5$ dex, and is not seen in metal-poor dSph stars, providing a potentially useful indicator for investigating chemical evolution.

The correlation between sodium and nickel content is the nucleosynthetic result of neutron capture in massive stars. As previously discussed, the total Na abundance is controlled by the neutron excess, which limits the production of ^{58}Ni during SN II events. When the inevitable supernova begins, the core photodissociates into neutrons and protons, allowing the temporary creation of ^{56}Ni before it decays to ^{56}Fe . A limited amount of ^{54}Fe is also formed, which is the main source of production for the stable ^{58}Ni isotope through α -capture. When the core dissociates, the quantity of ^{54}Fe (and hence ^{58}Ni) produced is dependent on the abundance of neutron-rich elements during the explosion. As ^{23}Na is a relatively plentiful neutron source with respect to other potential sources (like ^{13}C), the post-supernova ^{58}Ni abundance is driven by the pre-explosion ^{23}Na content. Re-

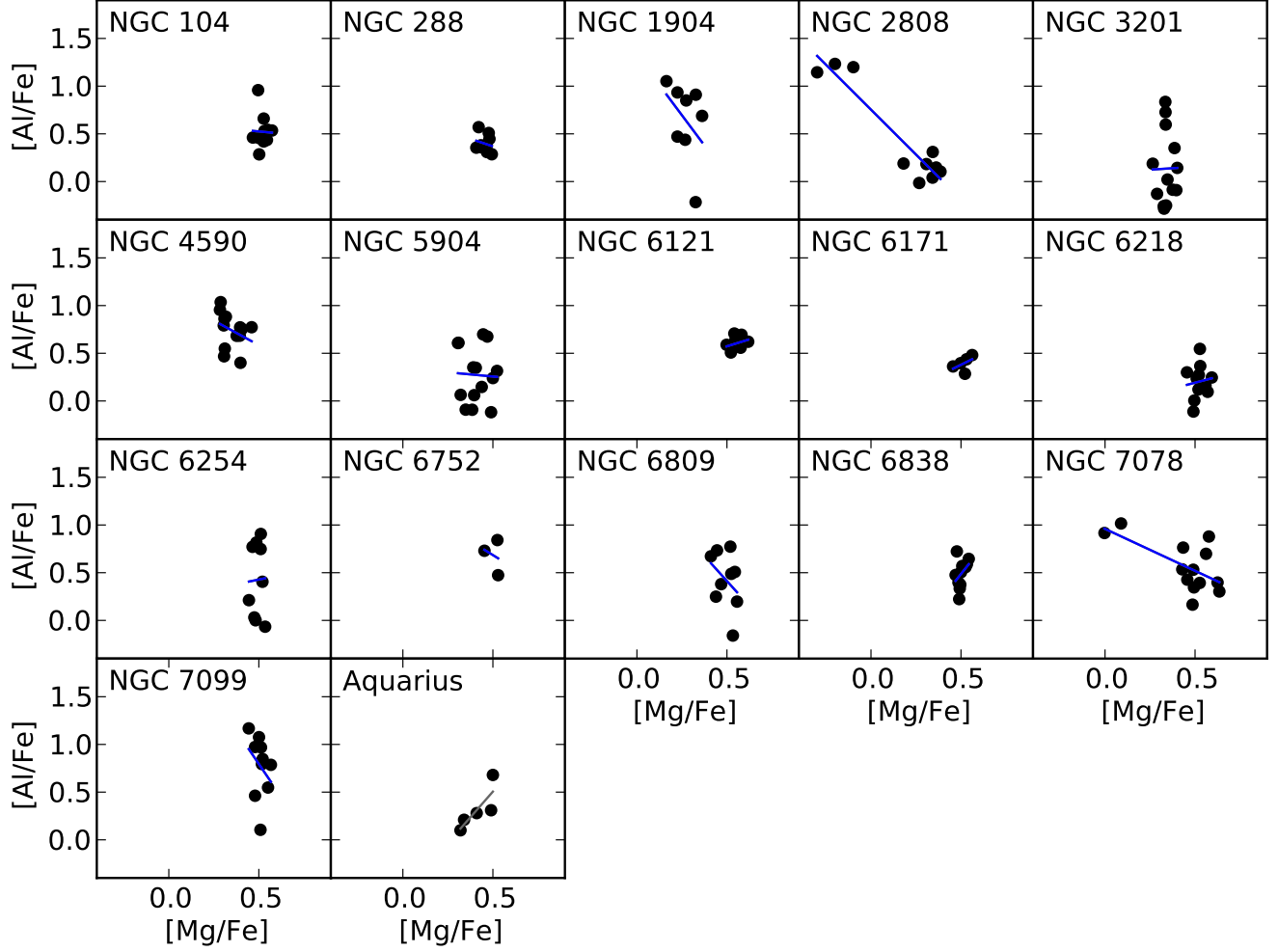


FIG. 10.— $[Mg/Fe]$ and $[Al/Fe]$ abundances for stars in 16 globular clusters from ? and for the five Aquarius stream candidates. The inverse Mg-Al correlation is illustrated, most obviously in NGC 2808 and NGC 1904. The strong positive correlation observed in Aquarius is in stark contrast with other classical globular clusters.

call that the total Na production primarily depends on the neutron excess. Thus, through populations of massive stars undergoing C-burning, a positive correlation between sodium and nickel can be expected.

Stars originating in dwarf spheroidal galaxies and globular clusters have very different chemical enrichment environments. Consequently, both types of systems exhibit chemistry that reflects their nucleosynthetic antiquity. Dwarf spheroidal stars do not demonstrate enhanced sodium or nickel content with respect to iron, as there has been a relatively negligible lineage of massive stars undergoing supernova. In contrast, globular cluster stars do have elevated $[Na/Fe]$, $[Ni/Fe]$ signatures. This sharp contrast between dwarf spheroidal and globular cluster star chemistry is illustrated in Figure 11. Given the extended star formation within the Milky Way disk, globular cluster stars and disk stars are indiscernible in the Na/Ni plane: they both show an extended contribution of massive stars. The most that can be inferred from the Na, Ni abundances of Aquarius stream stars is that their enrichment environment is less like a dSph galaxy, and more representative of a globular cluster, or the disc of the Milky Way.

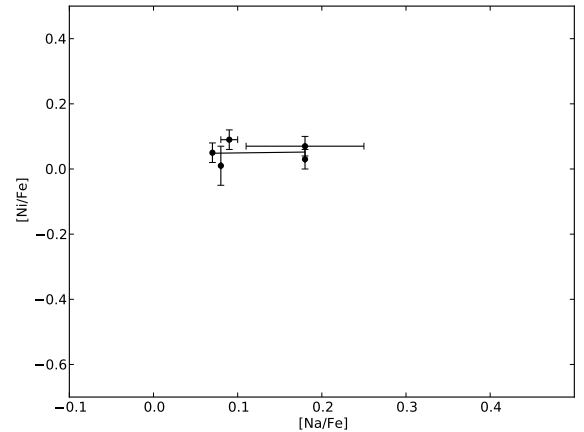


FIG. 11.— A plot showing $[Na/Fe]$ and $[Ni/Fe]$ for all Aquarius stream stars. TODO add dwarf/GC/disk stars on here.

4.6. The Chemical Distinctiveness of C2225316

C2225316 exhibits peculiar chemical abundances compared to the rest of the Aquarius candidates. It is overabundant in light refractory elements, and exhibits a

strong barium abundance of $[\text{Ba}/\text{Fe}] = 0.70$ dex. This abundance is well in excess of the halo ($[\text{Ba}/\text{Fe}] \sim 0.0$) – and our other Aquarius stream stars – which vary between -0.02 to 0.15 dex.

High s -process enhancements have been noted for a few disrupted globular clusters that exhibit a wide metallicity range. Most notably: ω Centurai (Majewski et al. 2012), M22 (Marino et al. 2011) and ($\#$ any others?). Like the Aquarius co-moving group, both clusters are relatively close to the sun: $R_{\odot} = 5.2$ kpc and 3.2 kpc, respectively. M22 has a mean metallicity of $[\text{Fe}/\text{H}] \sim -1.7$, varying between $-2.0 < [\text{Fe}/\text{H}] < -1.6$ dex. Since C2225316 has a metallicity of $[\text{Fe}/\text{H}] = -1.26$ dex, it is unlikely to be associated with M22. However, the high barium content and overall metallicity of C2225316 ($[\text{Fe}/\text{H}] = -1.26$) suggests there may be an association with ω -Centurai.

ω -Centurai has a retrograde orbit with low inclination. Many groups simulating this orbit have predicted retrograde tidal debris to occur near the Solar circle (Dinescu 2002; Tsuchiya et al. 2003, 2004; ?; Bekki & Freeman 2003). Subsequent searches for ω -Cen debris in the solar neighbourhood have led to tantalizing signatures of debris. From over 4,000 stars selected from the ω -Cen color-magnitude diagram by Da Costa & Coleman (2008), only six candidate members were recovered. More recently, Majewski et al. (2012) presented data from the Grid Giant Star Survey (GGSS), an all-sky search looking for metal-poor giant stars. From their data, they identified 12 stream candidates. Although this scarcity is consistent with tidal stripping occurring long ago, it is perhaps worrying that searches for stripped stars near ω -Cen itself have been even less fruitful.

In addition to presenting new stream candidates, Majewski et al. (2012) performed 4,050 different simulations in order to predict likely locations for tidal debris. The results of their simulation are replicated in Figure ??, where the location of C2225316 is also shown. Interestingly, the velocity and position of C2225316 line up almost precisely where Majewski et al. (2012) predict a high probability of stream members.

Although this is interesting from a qualitative perspective, the most striking evidence for an association with ω -Centurai is in chemistry. Figure ?? demonstrates the $[\text{Ba}/\text{Fe}]$ abundance for ω -Cen stars compared to that of the galactic halo. A steep Ba enhancement is present, which is unique to the globular clusters ω -Cen and M22. We note that although high s -process enrichment is present in other systems (IC 2391, the Argus association; De Silva et al. 2013), these systems are have metallicities near solar values and are unlikely to be associated with C2225316.

The chemical peculiarity of C2225316 suggests that it is distinct from the Aquarius co-moving group. The high s -process enrichment is similar to that observed in ω -Centurai stars, and the overall metallicity ($[\text{Fe}/\text{H}] = -1.26$) agrees excellently with the mean metallicity of a known sub-population within ω -Centurai. Moreover, the position and velocity for C2225316 precisely coincide with the most likely predictions for tidal debris from ω -Centurai. The chemical and phase-space information indicates that C2225316 is likely associated with the disrupted globular cluster ω -Centurai.

4.7. Possible Progenitors

Since the Aquarius stream is kinematically coherent, the default assumption is that the system has been accreted. The stream candidates presented here are slightly enhanced in sodium and nickel, suggesting that if a progenitor ever existed then its environment was more like a globular cluster than a dSph galaxy. Based on a lack of α -enhancement and increased $[\text{Na}/\text{Fe}]$, $[\text{Ni}/\text{Fe}]$ abundances, we exclude the possibility that the Aquarius stream has resulted from a disrupted dwarf satellite. If the progenitor is a disrupted globular cluster, and all our candidates are members, then it has a wider metallicity distribution than most globular clusters.

However, our chemical analysis does not reveal any inverse Na-O correlation – which would be strong evidence for a globular cluster environment. Furthermore, we observe a positive Mg-Al relationship, the same seen by Wylie-de Boer et al. (2012). High resolution, high S/N spectra for the entire stream may be required before such chemical signatures may become apparent. In this section we discuss other possible causes for the Aquarius co-moving group.

4.7.1. ω -Centurai

In their original discovery paper, Williams et al. (2011) attempted to exclude possible known progenitors. On the basis of metallicity, distance, proper motions⁶, transverse velocities and orbital energies, the authors were able to exclude all known Milky Way satellites, with the notable exception of ω -Centurai. Although the Aquarius stream metallicity distribution we find is not dissimilar from a known sub-population in ω -centurai, the individual chemical abundances are quite distinct. ω -Centurai members exhibit a strong s -process enhancement with overall metallicity. This signature is not observed in our data, with the exception of C2225316, which seems to be chemically distinct from the other Aquarius group candidates.

Due to our limited sample size, it is impossible to know whether C2225316 is an outlier, or our four other candidates are halo interlopers. Either position is debatable, and both lead to interesting interpretations. If most of our observed candidates are halo members, and C2225316 represents the Aquarius stream chemistry, then an association between Aquarius and ω -Centurai is possible.

4.7.2. Disrupted Disk Stars – Signature of a Minor Merger

- # Velocity distribution wide
- # Spatial distribution wide
- # Chemistry rules out a dSph origin
- # No signs of classical GC chemical patterns
- # The stream chemistry is indistinguishable from disk stars in every aspect
- # Revised distances to each star, transverse motions + orbital energies calculated
- # Monte-carlo simulations demonstrate strongly retrograde stars wrt thick disk + halo

⁶ The proper motions in Table 1 of Williams et al. (2011) are mis-associated to incorrect stars. However, this error was typographical; it did not affect the transverse velocity calculations (Williams, M.E.K, private communication).

Orbital energy pattern aligns exactly with Zolotov+ simulations, but would require a smaller mass of the disrupter (minor merger)

Need to discuss disk is unlikely to have had a merger in past 8 Gyr

5. CONCLUSIONS

Conclusions

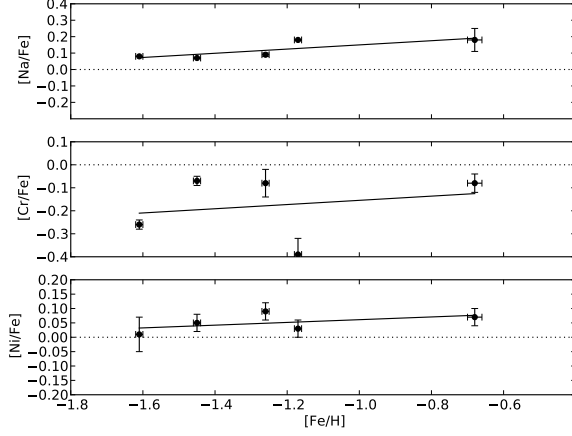


FIG. 12.— A plot showing $[Na/Fe]$, $[Cr/Fe]$, and $[Ni/Fe]$ for all Aquarius stream stars.

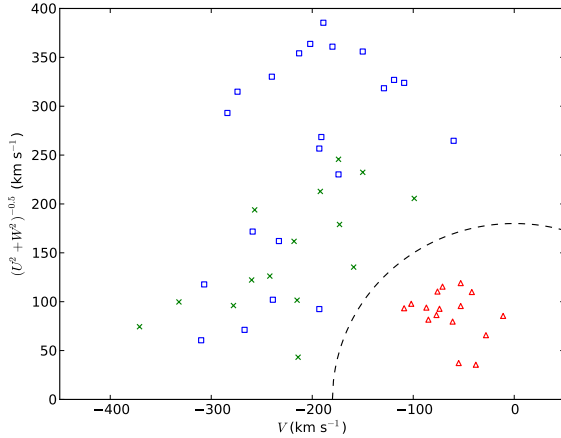


FIG. 13.— Toomre plot.

A.R.C. acknowledges the financial support through the Australian Research Council Laureate Fellowship 0992131, and from the Australian Prime Minister's Endeavour Award Research Fellowship, which has facilitated his research at MIT. This publication makes use of data products from the Two Micron All Sky Survey, which is a joint project of the University of Massachusetts and the Infrared Processing and Analysis Center/California Institute of Technology, funded by the National Aeronautics and Space Administration and the

REFERENCES

- Allende Prieto, C., Lambert, D. L., & Asplund, M. 2001, *ApJ*, 556, L63
- Alonso, A., Arribas, S., & Martínez-Roger, C. 1999, *A&AS*, 140, 261
- Aoki, W., et al. 2007, *ApJ*, 660, 747
- Arnould, M., Goriely, S., & Jorissen, A. 1999, *A&A*, 347, 572
- Asplund, M., & García Pérez, A. E. 2001, *A&A*, 372, 601
- Asplund, M., Grevesse, N., Sauval, A. J., & Scott, P. 2009, *ARA&A*, 47, 481
- Barber, C., Dobkin, D., & Huhdanpaa, H. 1996, *ACM Transactions on Mathematical Software (TOMS)*, 22, 469
- Baumüller, D., & Gehren, T. 1997, *A&A*, 325, 1088
- Bekki, K., & Freeman, K. C. 2003, *MNRAS*, 346, L11
- Belokurov, V., et al. 2007, *ApJ*, 658, 337
- Bernstein, R., Sackett, S. A., Gunnels, S. M., Mochnacki, S., & Athey, A. E. 2003, in *Society of Photo-Optical Instrumentation Engineers (SPIE) Conference Series*, Vol. 4841, Society of Photo-Optical Instrumentation Engineers (SPIE) Conference Series, ed. M. Iye & A. F. M. Moorwood, 1694–1704
- Burris, D. L., Pilachowski, C. A., Armandroff, T. E., Sneden, C., Cowan, J. J., & Roe, H. 2000, *ApJ*, 544, 302
- Carretta, E., et al. 2009, *A&A*, 505, 117
- Casagrande, L., Ramírez, I., Meléndez, J., Bessell, M., & Asplund, M. 2010, *A&A*, 512, A54
- Castelli, F., & Kurucz, R. L. 2003, in *IAU Symposium*, Vol. 210, *Modelling of Stellar Atmospheres*, ed. N. Piskunov, W. W. Weiss, & D. F. Gray, 20P
- Cayrel, R., et al. 2004, *A&A*, 416, 1117
- Da Costa, G. S., & Coleman, M. G. 2008, *AJ*, 136, 506
- De Silva, G. M., D'Orazi, V., Melo, C., Torres, C. A. O., Gieles, M., Quast, G. R., & Sterzik, M. 2013, *ArXiv e-prints*

- Dinescu, D. I. 2002, in *Astronomical Society of the Pacific Conference Series*, Vol. 265, *Omega Centauri, A Unique Window into Astrophysics*, ed. F. van Leeuwen, J. D. Hughes, & G. Piotto, 365
- Drake, A. J., et al. 2013, *ArXiv e-prints*
- Frebel, A., Simon, J. D., Geha, M., & Willman, B. 2010, *ApJ*, 708, 560
- Freeman, K., & Bland-Hawthorn, J. 2002, *ARA&A*, 40, 487
- Fulbright, J. P. 2000, *AJ*, 120, 1841
- García Pérez, A. E., Asplund, M., Primas, F., Nissen, P. E., & Gustafsson, B. 2006, *A&A*, 451, 621
- Gratton, R. G., & Sneden, C. 1991, *A&A*, 241, 501
- Gratton, R. G., Sneden, C., Carretta, E., & Bragaglia, A. 2000, *A&A*, 354, 169
- Grevesse, N., & Sauval, A. J. 1998, *Space Sci. Rev.*, 85, 161
- Helmi, A., & White, S. D. M. 1999, *MNRAS*, 307, 495
- Hinkle, K., Wallace, L., Livingston, W., Ayres, T., Harmer, D., & Valenti, J. 2003, in *The Future of Cool-Star Astrophysics: 12th Cambridge Workshop on Cool Stars, Stellar Systems, and the Sun*, ed. A. Brown, G. M. Harper, & T. R. Ayres, Vol. 12, 851–856
- Majewski, S. R., Nidever, D. L., Smith, V. V., Damke, G. J., Kunkel, W. E., Patterson, R. J., Bizyaev, D., & García Pérez, A. E. 2012, *ApJ*, 747, L37
- Marino, A. F., et al. 2011, *A&A*, 532, A8
- Munari, U., Sordo, R., Castelli, F., & Zwitter, T. 2005, *A&A*, 442, 1127
- Munari, U., & Zwitter, T. 1997, *A&A*, 318, 269
- Nataf, D. M., et al. 2012, *ArXiv e-prints*
- Nissen, P. E., Chen, Y. Q., Schuster, W. J., & Zhao, G. 2000, *A&A*, 353, 722
- Nissen, P. E., & Schuster, W. J. 1997, *A&A*, 326, 751
- . 2011, *A&A*, 530, A15
- Norris, J. E., & Da Costa, G. S. 1995, *ApJ*, 441, L81
- Norris, J. E., Ryan, S. G., & Beers, T. C. 1996, *ApJS*, 107, 391
- Peek, J. E. G., & Graves, G. J. 2010, *ApJ*, 719, 415
- Reddy, B. E., Tomkin, J., Lambert, D. L., & Allende Prieto, C. 2003, *MNRAS*, 340, 304
- Robin, A. C., Reylé, C., Derrière, S., & Picaud, S. 2003, *A&A*, 409, 523
- Schlegel, D. J., Finkbeiner, D. P., & Davis, M. 1998, *ApJ*, 500, 525
- Sharma, S., Bland-Hawthorn, J., Johnston, K. V., & Binney, J. 2011, *ApJ*, 730, 3
- Shetrone, M. D. 1996, *AJ*, 112, 1517
- Siebert, A., et al. 2011, *AJ*, 141, 187
- Sneden, C. A. 1973, PhD thesis, The University of Texas at Austin.
- Sobeck, J. S., et al. 2011, *AJ*, 141, 175
- Steinmetz, M., et al. 2006, *AJ*, 132, 1645
- Tsuchiya, T., Dinescu, D. I., & Korchagin, V. I. 2003, *ApJ*, 589, L29
- Tsuchiya, T., Korchagin, V. I., & Dinescu, D. I. 2004, *MNRAS*, 350, 1141
- Williams, M. E. K., et al. 2011, *ApJ*, 728, 102
- Woosley, S. E., & Weaver, T. A. 1995, *ApJS*, 101, 181
- Wylie-de Boer, E., Freeman, K., Williams, M., Steinmetz, M., Munari, U., & Keller, S. 2012, *ApJ*, 755, 35
- Yong, D., Carney, B. W., & Teixeira de Almeida, M. L. 2005, *AJ*, 130, 597
- Zwitter, T., et al. 2008, *AJ*, 136, 421